5-2012

Characterization and optimization of solution-derived chalcogenide glass thin films

Jacklyn Wilkinson
Clemson University, jmnovak727@gmail.com

CHARACTERIZATION AND OPTIMIZATION OF SOLUTION-DERIVED CHALCOGENIDE GLASS THIN FILMS

A thesis
Presented to
the Graduate School of
Clemson University

In Partial Fulfillment
of the Requirements for the Degree
Master of Science
Materials Science and Engineering

---

by
Jacklyn Wilkinson
May 2012

Accepted by:
Dr. Kathleen Richardson, Committee Chair
Dr. John Ballato
Dr. Igor Luzinov
Dr. Marc Dussauze
Dr. Nathan McClenaghan

ABSTRACT

Chalcogenide glasses have many unique properties that allow them to be used in a variety of optical applications. Infrared transparency allows them to be used in sensors for molecules that have "fingerprints" in the 2-25 μm range. By producing amorphous thin films of these materials, they can be incorporated into chemical sensors as planar waveguides and resonators. The goal of this work was to fabricate and characterize solution-derived chalcogenide thin films for use in chemical sensors with a source wavelength between 3-3.5 μm.

The structural and optical properties of the parent bulk glass were characterized and used as reference for the solution-derived thin film studies. Thermally evaporated thin films have been routinely used in chemical sensor geometries in our group and were used as a point of reference for the target roughness and surface quality of the spin-coated films. The goal was to produce films with the same structure and optical properties as the bulk glass, roughness equal to or less than TE films, and a surface free of cracks and pinholes. Glass thin films in the Ge-Sb-S family were deposited using the spin-coating method. The glass solutions were optimized by studying the effects of water content and glass loading on the post-processed films. This work has shown that the water content of the solvent influences glass dissolution and that glass loading is the key parameter for controlling film thickness. The removal of residual solvent was studied using in-situ FTIR measurements during heat treatments at various temperatures. Changes in the glass structure and solvent-glass interactions were studied through detailed analysis of the far-IR and mid-IR regions, respectively. Strong glass-solvent interactions were shown to

exist and temperatures well above the boiling point of the solvent were needed to remove it. For each temperature, correlations were made between structural aspects and properties such as refractive index measured by ellipsometry, band gap by UV-vis absorption, and surface roughness by AFM. These properties were shown to be affected not only by residual solvent, but also by pores left as the solvent was removed and by consolidation of the film as the pores were eliminated.

DEDICATION

This thesis would not have been possible without the support of many people. First, I would like to thank my husband, Spencer, for his love and encouragement as well as his help with my experiments. I couldn't have done it without him! I would also like to thank the rest of my family, who are always there to support me.

This wouldn't have been possible without the guidance of my advisor at Clemson, Dr. Kathleen Richardson. I have become a better researcher and a better writer because of her. I would also like to thank her, and Dr. Evelyne Fargin, for the opportunity to participate in the Atlantis-MILMI program and to study at the University of Bordeaux 1. Living and studying in Bordeaux has been a great experience. Also thanks to Marc Dussauze, my advisor in Bordeaux, for all of his help. Many of my experiments have been made possible thanks to his expertise. Thanks to the faculty and staff at both universities for all of their help along the way.

Finally, thanks to all of my group members. They have helped in many ways and kept me motivated in my classes and research. I am grateful for all of their contributions.

ACKNOWLEDGMENTS

I would like to acknowledge the United States Department of Energy (DoE) for partial funding of this research, which was conducted under project #DE-000421, entitled "Compact, highly sensitive and selective Mid-Infrared (MIR) chemical sensors." This project was conducted as part of a collaborative effort between Clemson University, the Massachusetts Institute of Technology, and Physical Sciences, Inc.

The Atlantis-MILMI (Master International in Laser, Materials Science, and Interaction) program also provided partial funding. The MILMI master is funded by the Atlantis program, which supports the cooperation between EU and US higher education institutions. Funding support is both provided by the Department of Education of the United States Government under the contract #P116J080033, University of Central Florida and the European Commission under the contract #2008-1750/001-001 CPT-USTRAN, Université Bordeaux 1.

I would also like to thank my collaborators on other aspects of this work. Thank you to Vivek Singh at MIT for depositing thin films by thermal evaporation for me to use as a reference material for my solution-derived thin film studies. Thank you to Frédéric Adiametz at the University of Bordeaux 1 for his support in using ellipsometry to measure the refractive index of my samples. Colette Belin, also at the University of Bordeaux 1, provided AFM measurements.

TABLE OF CONTENTS

Page

Table of Contents (Continued)

Page

LIST OF TABLES

LIST OF FIGURES

List of Figures (Continued)

Figure Page

List of Figures (Continued)

Figure Page

List of Figures (Continued)

Figure Page

List of Figures (Continued)

Figure Page

CHAPTER ONE

MOTIVATION AND RESEARCH OBJECTIVES

1.1 Motivation

Previous studies have demonstrated that chalcogenide glass (ChG) thin films produced by thermal evaporation (TE) can be fabricated into waveguides and resonators for use in chemical sensors [1,2]. A solution-based approach to fabricating ChG thin films has been explored as an alternative to thermal evaporation [3]. An advantage of solution-based processing is that the films can be made at lower temperatures, reducing energy costs associated with the high temperatures needed for TE. Lower temperatures also mean that the harmful elements in the glass do not need to be volatilized. While some initial research on solution-derived ChG thin films has been obtained previously [3], many questions remain unanswered. In this thesis, an attempt to further the understanding of the structure of the thin films and to correlate changes in the structure with changes in optical and physical properties at each step of the film synthesis has been carried out.

1.2 Research Objectives

The goal of this work has been to fabricate and characterize solution-derived chalcogenide thin films for use in chemical sensors where the source wavelength is in the 3-3.5 μm range. The films would be used as planar waveguides and resonators. Previous work for sensors with a source wavelength of 1550 nm used thermally evaporated films with a thickness of 450 nm [1]. The thickness of the films must be increased to ~800 nm for use at 3-3.5 μm. In order to have low optical loss, the surface roughness of the films

should be low (a few nm (rms) or less) and there should be little to no surface defects such as pinholes and cracking.

Ultimately, the goal is to be able to fabricate solution-derived chalcogenide thin films that have properties matching those of the parent bulk glass. However, due to being fabricated by a solution-derived method, the deposited films are made up of a combination of glass and solvent. The solvent has significantly different optical properties than the glass and is undesirable in the final film. Thus, a specific focus of process optimization is to successfully remove the maximum amount of solvent using the most appropriate time/temperature protocol, to maximize resulting film quality in the desired thickness. For this reason, the main focus of this research has been on residual solvent removal and the influence of that process on final film quality and structure. Glass-solvent interactions and how these interactions, as well as the structure of the glass network itself change during solvent removal, is influenced by the specifics of the heat treatment process. In this investigation, each of these effects combined with structural characterization, have been correlated to optical and physical properties of the films.

The main questions addressed in this thesis are:

1. How does water affect the glass solutions and the resulting quality and structure of spin-coated films?
2. How can most, if not all, of the residual solvent be removed from the films? What heat treatment times and temperatures are necessary and how do these variables influence post-processed film quality and properties?

3. How does the solvent interact with the glass network and how do these interactions change as solvent is removed?
4. How does residual solvent affect the optical (refractive index, band gap) and physical (roughness, thickness, surface quality) properties of the resulting post-processed films?

In the next chapter, the basic properties of chalcogenide glasses, why these properties make them ideal for use in chemical sensors, and the state of the art in this field, will be presented. This is followed by a description of the experimental methods used in this study. The results are discussed beginning in Chapter 4 with the characterization of the bulk glass and thermally evaporated films, which will be used as reference materials that will serve as the target properties for the solution-derived thin films. Optimization of the glass solutions is presented in Chapter 5. In Chapter 6, changes in the structure of the thin films with solvent removal are characterized and correlated to changes in the optical and physical properties. Finally, conclusions and future work are presented.

1.3 References

1. Hu J, Carlie N, Feng N-N, Petit L, Agarwal A, Richardson K, and Kimerling L. Planar waveguide-coupled, high-index-contrast, high-Q resonators in chalcogenide glass for sensing. *Optics Letters*. **33**(21), 2500-2502 (2008).
2. Hu J, Tarasov V, Agarwal A, Kimerling L, Carlie N, Petit L, and Richardson K. Fabrication and testing of planar chalcogenide waveguide integrated microfluidic sensor. *Optics Express*. **15**(5), 2307-2314 (2007).
3. Carlie N. A solution-based approach to the fabrication of novel chalcogenide glass materials and structures. PhD Thesis. Clemson University (2010).

CHAPTER TWO

INTRODUCTION

Chalcogenide glasses (ChGs) have unique properties that make them ideal for use in optical biosensors. In this chapter, the basic properties of ChGs and how these properties relate to sensing applications will be explored. A description is also given of all-integrated microphotonic technology and how chalcogenides can be utilized in these devices as waveguides and planar resonators. Different thin film deposition techniques will be compared and the state of the art in microphotonic chalcogenide sensors will be presented.

2.1 Basic Properties of Chalcogenide Glasses

Chalcogenide glasses are amorphous materials that contain one or more of the chalcogen elements, which include sulfur (S), selenium (Se), and tellurium (Te), and are found in group 16 of the periodic table. Oxides are a separate group of materials and are not considered chalcogenides even though oxygen is a chalcogen. The chalcogen elements are covalently bonded with network formers such as arsenic (As), germanium (Ge), gallium (Ga), antimony (Sb), etc to form the glass structure. This structure can be defined as a "continuous random network" (CRN) because, unlike a crystalline material, it does not exhibit long-range order [1]. A comparison of the structures of a crystal and a glass is shown in Figure 2.1 below.

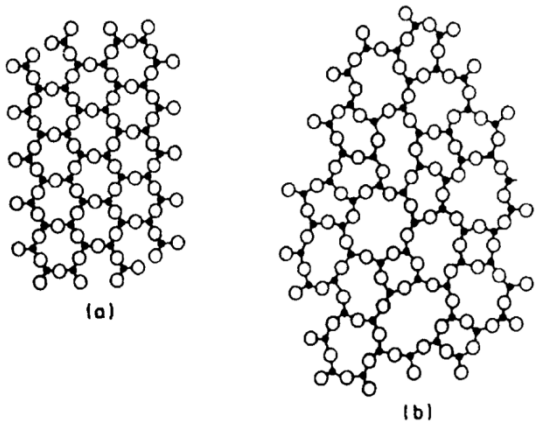

Figure 2.1: Structure of (a) A_2O_3 crystal and (b) A_2O_3 glass, taken from reference [1].

The figure depicts the structure of an oxide glass but the CRN theory can also be applied to chalcogenides. The glass structure is "continuous" because it is a vast network rather than just a few atoms and it is "random" because it lacks the repeating, periodic structure that the crystal exhibits [1]. As shown in the figure, all of the A-O-A bond angles are the same in a crystal but these bond angles are varied in a glass, which brings about disorder. When melting a single chalcogen, such as pure S or pure Se, rings are formed as the material is melted and then the rings open and polymerize into long chains, which form a glass if the material is rapidly quenched [2]. Adding elements with higher coordination numbers, such as Ge or As, increases the connectivity and creates a more 3D network by crosslinking the chains as illustrated in Figure 2.2 below [2-3].

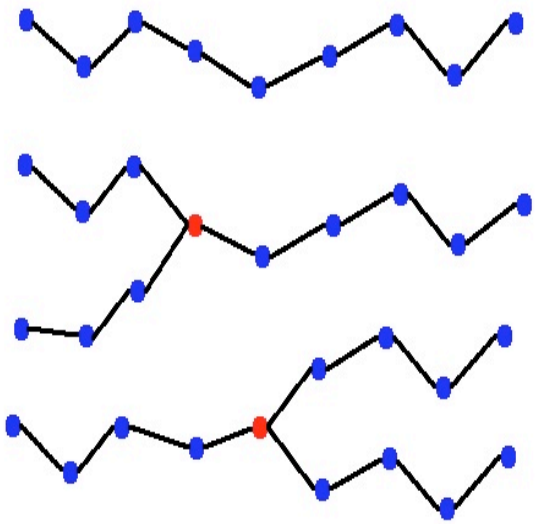

Figure 2.2: Illustration of the structure of S or Se (blue circles) glass with a small amount of As (red circles).

The coordination number is equal to 8-N where N is the number of electrons in the outer shell and the average coordination number for the atoms in a glass will be designated as $< r >$. Thorpe [4] drew some general conclusions about chalcogenide glasses based on the value of $< r >$. He argued that ChGs were a combination of "rigid" and "floppy" regions. A "floppy" material, such as a polymer made up of chains, is deformed easily while a "rigid" material such as silicon is not [4]. The main conclusion of Thorpe's work is that a glass with a low $< r >$ value, called a "polymeric glass," is made up of small rigid regions contained within an otherwise floppy network. The size of these regions grows as $< r >$ increases, until the structure becomes that of an "amorphous solid" when $< r > = 2.4$, where small floppy regions are contained in a rigid network [4]. Figure 2.3 depicts the differences between a polymeric glass and an amorphous solid based on the work of Thorpe.

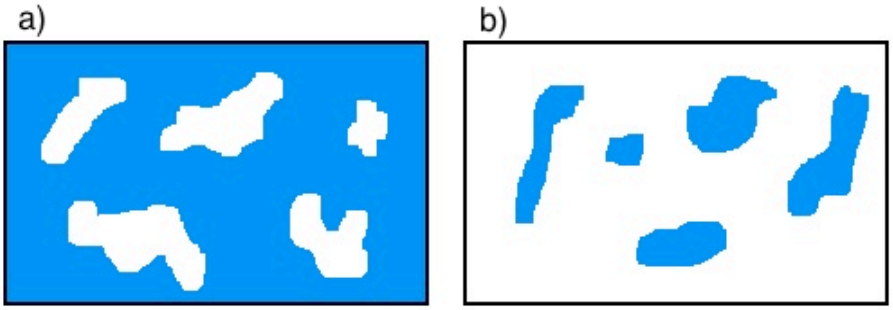

Figure 2.3: Illustration of a polymeric glass (a) and an amorphous solid (b). The white areas represent the "rigid" regions and the blue areas represent the "floppy" regions.

The three compositions that will be discussed in this thesis, As_2S_3, $Ge_{23}Sb_7S_{70}$, and $Ge_{23}Sb_4S_{73}$, have $< r >$ values of 2.4, 2.53, and 2.5, respectively. This means that all of the compositions are amorphous solids, with $Ge_{23}Sb_7S_{70}$ being the most rigid. While there are also other factors that determine the glass transition temperature, or T_g, the $< r >$ value helps to predict that $Ge_{23}Sb_7S_{70}$ will have the highest T_g ($T_g \approx 311°C$) and As_2S_3 will have the lowest ($T_g \approx 200°C$).

Chalcogenide glasses exhibit poor transparency in the visible region and some compositions even appear black [5]. However, the absence of oxygen allows these glasses to have a large transparency window in the infrared region [6]. As seen in Figure 2.4, glasses in the three chalcogenide families of sulfides, selenides, and tellurides are transparent at much higher wavelengths than silica and ZBLAN (a fluoride glass). Other interesting optical properties displayed by ChGs include nonlinearity and photosensitivity [5-8]. ChGs have high densities compared to oxide glasses and they also have high refractive indices of $n \approx 2\text{-}3$ [6-7].

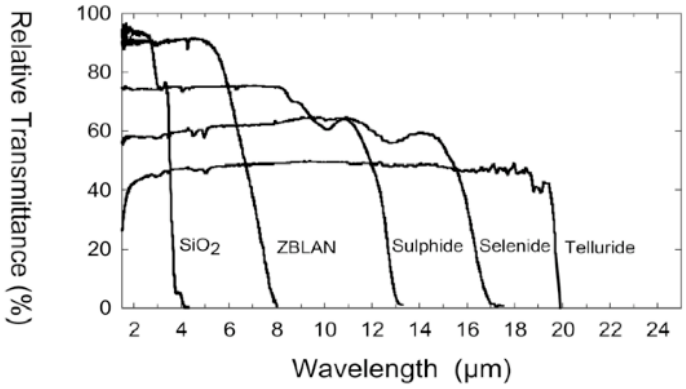

Figure 2.4: Transmission spectra for several glasses (2-3 mm thick), taken from reference [9]

Chalcogenide glasses have very wide glass forming regions and are easily doped by other elements such as rare earth ions [7-8,10-11]. Figure 2.5 shows the glass forming regions for some typical ternary chalcogenide glasses, where "Ch" represents the chalcogen element: S, Se or Te.

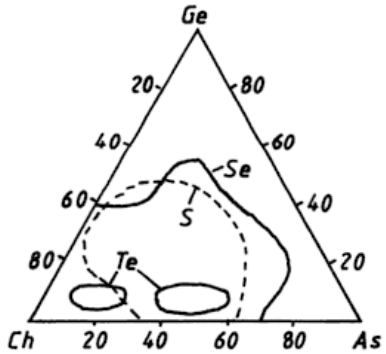

Figure 2.5: Glass forming regions in the system Ge-As-Ch, taken from reference [12]

Having a wide composition region allows the properties of ChGs to be adjusted and optimized for different applications just by changing the composition. For example, Ge-based glasses are more rigid and have higher glass transition (T_g) and melting (T_m) temperatures than As-based glasses [7]. Germanium is a four-coordinated network

former, so the glass structure becomes stronger and more connected when germanium is added.

2.2 Why Chalcogenides for Sensors?

As mentioned previously, chalcogenide glasses have a broad glass forming region, are resistant to crystallization and thus can be fabricated in bulk form, thin film or fiber form, and lastly, possess a large transparency window in the infrared region. This allows them to be used in sensors for many molecules, often organic, that have "fingerprints" in the 2-25 μm range [5-7]. These "fingerprints" are characteristic infrared absorption bands associated with molecules due to their fundamental vibrational modes. Just like each person has their own unique set of fingerprints, many chemicals have their own unique absorption spectra that can be used to identify them. The spectra of benzene, toluene, and a mixture of 50% of each are shown in Figure 2.6 below. As can be seen in the figure, each species has its own distinct absorptions in the 8-11.5 μm spectral region and the mixture has characteristics of both. As was previously discussed in reference to Figure 2.4, chalcogenide glasses are transparent in this region. Oxide and fluoride glasses are not transparent at wavelengths higher than about 4 and 8 μm, respectively. For this reason, they would be unsuitable materials for sensing organic molecules. Another advantage is that, because ChGs are transparent in the near-IR, where water is optically transparent, they can be used to sense molecules in aqueous environments without water disrupting the signal [7]. This is especially important for sensing biological molecules, which are most often found in an aqueous environment.

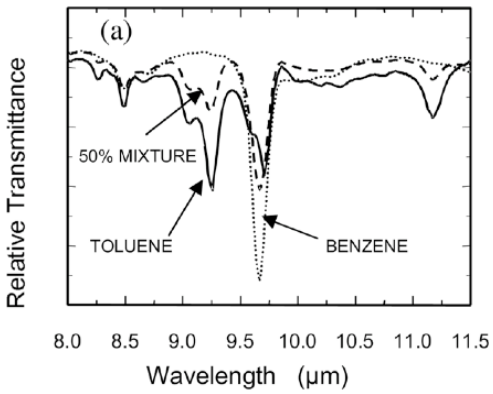

Figure 2.6: IR spectra of some organic species, taken from reference [9]

Chalcogenide glass sensors can be used to detect a wide variety of chemicals. Some ChG sensors monitor changes in electrical properties such as potential. In this way, they can be used for sensing sulfur species for applications such as detecting hydrogen sulfide in wastewater treatment processes and in seawater [10]. Another application of ChG sensors is detecting metal ions, such as copper and iron, in the water at nuclear plants in order to monitor corrosion processes [13]. However, the focus in this report will be on optical sensors. In addition to monitoring many of the chemical species described above, ChG sensors can also be used to sense biological macromolecules, such as proteins and nucleic acids, which is beneficial in clinical diagnostics, macro-molecular drug discovery, and anti-bioterrorism [7].

The ability to produce ChGs in fiber and thin film form also makes them attractive for sensing applications [6,9]. This gives them the flexibility to be used in different kinds of sensors. Sensors using ChG fibers have the potential to be used as a "fiber optic dipstick probe" to check the quality of engine oil or for other purposes such as detecting soil contaminants [9]. Planar waveguides are better suited for some

applications because they can be smaller and can be integrated into “lab-on-a-chip” type devices [6]. Whereas metal oxide sensors often must operate in excess of 300°C to sense chemicals by detecting conductance changes, ChG sensors can operate at room temperature, eliminating the need for heating the sensors [14]. The ChG sensors have been shown to exhibit a short response time and good sensitivity [14]. All of these properties make them very attractive as materials to be used in sensors.

For a fiber sensor, the fiber is both the waveguide and the sensing element but, for a planar waveguide, a resonator can be added in addition to the waveguide. The sensitivity of a fiber sensor has been shown to increase when the diameter of the fiber decreases, so one way to increase the sensitivity of fiber sensors is to taper the fiber in the sensing zone [15-16]. This is because it increases the number of reflections in the fiber, so the light interacts with the analyte more. While this increases the sensitivity to a certain extent, it is still limited by the small interaction region. By using a planar sensor, the light goes around the resonator multiple times, which increases the interaction with the analyte and, therefore, increases the sensitivity. This allows the sensitivity to be increased without increasing the size of the device. Another way to improve the performance of the sensor is to modify the surface, usually by grafting a polymer, in order to enhance its specificity. Recent efforts on specificity-enhancing functionalized polymers for use in ChG-based planar sensors are discussed in [REF]. While it is relatively easy to graft polymers to the surface of a planar resonator, fibers cannot easily be made selective. Surface engineering of planar resonators will be discussed in more detail in section 2.3.2.

There are also some drawbacks to using ChGs as sensors. For example, they are toxic due to the presence of elements such as arsenic. This makes them unsuitable for many medical applications that they might otherwise be used in. Many of these glasses, especially in the As-S, As-Se, and As-S-Se systems, have a low T_g near 200°C [7]. This limits their use to low- to modest-temperature applications. In our team's most recent work, Ge has been added to the glass at the expense of As, to not only remove As, but to increase the glass transition temperature, enhance thermal stability, tailor refractive index and to yield more stable and highly process-able, thermally evaporated thin films. Compared to oxides, ChGs exhibit very low thermal and mechanical robustness [7-8]. Although they have optical properties that make them very attractive for sensing applications, the low stability and thermo-mechanical robustness of ChGs can limit their usefulness.

2.3 All-Integrated Microphotonic Technology

All-integrated microphotonic technology is the miniaturization of all of the parts that make up a device so that the entire system can fit on a small chip. One example of this is technology is an on-chip integrated chemical sensor. This system can be referred to as a "lab-on-a-chip" or a "sensor-on-a-chip." A schematic of an on-chip integrated chemical sensor is shown in Figure 2.7 below.

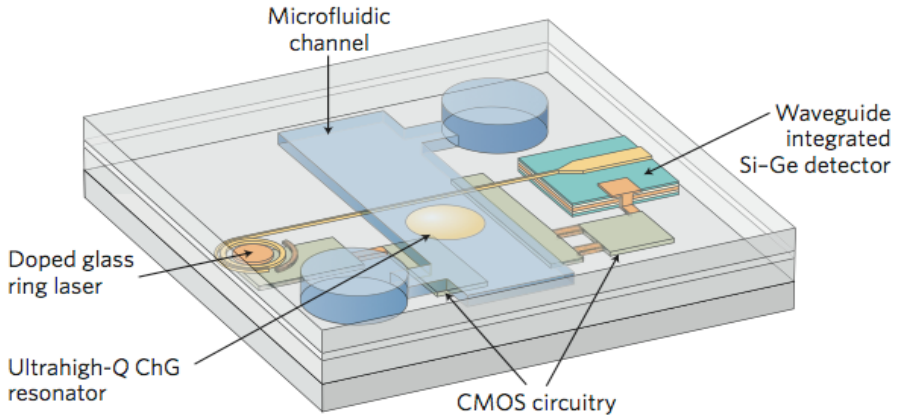

Figure 2.7: Schematic of a "lab-on-a-chip" sensing device, taken from reference [6].

Four basic components are needed to make the envisioned "lab-on-a-chip" sensor. These components are described in [7] and are the following:

1. Light source – The light source emits the probing light. In the schematic shown in the figure, the envisioned *integrated* (on chip) source is the doped glass ring laser. Our team is also investigating quantum-dot doped ChG sources [REF]. For this work, the glass films have been developed based on use of an off-chip, Inter-cascade Laser (ICL) with an emission wavelength between 3-3.5 μm.
2. Planar waveguides – The ChG waveguides couple the light from the source into the resonator and thus must have low loss at the probe wavelength.
3. Resonator – This is where strong interactions take place between the probing light and the analyte(s) via evanescent coupling. The ChG resonator's frequency (wavelength) is modified by the presence and/or binding of the analyte which results in either attenuation of the input signal (due to

absorption loss induced by binding), a shift in frequency of the resonator wavelength (due a modification of the refractive index), or both.

4. Detector – The IR detector receives the final signal which emanates from the resonator. This signal undergoes analysis for changes associated with the binding event and is compared to the initial probe to quantify the 'sensing' event.

Other components can also be added, such as the microfluidic channel shown in the figure. This channel is where the liquid or vapor containing the analyte enters the sensor and passes over the resonator. As the light travels through the waveguides and resonator, some of the light is absorbed by the analyte. The detector collects the optical signal following interaction within the resonator and the analyte can be identified by the characteristic attenuation and/or peak shift in the probe signal, since the glass is transparent in this region.

The next section discusses various techniques for depositing thin films, which can be fabricated into planar waveguides and resonators. This is followed by a detailed discussion of planar resonators, including modification of the surface.

2.3.1 Chalcogenide Thin Films: Deposition and Properties

Chalcogenide glass thin films can be fabricated by a number of techniques, including: thermal evaporation (TE), pulsed laser deposition (PLD), chemical vapor deposition (CVD), sputtering, and spin coating. TE involves heating glass powder until it vaporizes and then condenses on a cool substrate to form a film [8,17]. PLD is similar except a laser is used to vaporize material from a bulk target and then the vapor

condenses on the substrate [8,18-19]. In the CVD process, gaseous precursors react on the substrate and a film is formed [20-21]. Sputtering involves bombarding the surface of the target material with energetic particles, knocking loose some atoms from the target, which are then scattered and condense on the substrate [22-23]. For solution-based processing, films can be formed by either spin or dip coating. Here, glass powder is dissolved in an organic solvent and then the solution is either dipped into, or dripped onto a substrate, spun into a film, and then heat treated to drive off the solvent [24-25]. A more detailed description of each of these techniques and their advantages and disadvantages can be found in the appendix.

An advantage of the solution-based processing route is that it reduces energy costs associated with the high vacuum and temperatures used for thermal evaporation and the lasers used for pulsed laser deposition. Because of the lower temperatures, it is also more environmentally friendly because the harmful ingredients of the glass do not need to be volatilized. It can be difficult to control film composition with the thermal evaporation method because of different components volatilizing at different temperatures, but with solution-based processing the components are not volatilized so the composition should be easier to control. Another advantage of solution-derived films is the ability to quickly coat large surface areas. A major disadvantage is that it is difficult to remove all of the solvent from the film. The solvents typically absorb in the infrared so they can be a major source of loss in the film. One of the focuses of this work will be to study the effects of the solvent on the film properties and to propose a heat treatment that will allow the removal of as much solvent as possible.

The structural and optical properties of thin films produced by these various techniques differ from each other and *differ from the bulk glass*. The composition, refractive index, band gap, and structure of the glass network can vary between different film deposition techniques. It is possible to deposit films that will have some properties that match the bulk but there will always be differences. For example, films deposited by PLD have been shown to have the same composition as the bulk glass but Raman spectroscopy shows that the structure differs as well as the optical properties [8]. The glass structure is not only linked to composition but also to thermodynamic history such as the quenching rate, which differs depending on the fabrication process. It is important to link composition, structure, *and* optical properties. Thin films have different properties depending on the fabrication process used and they will never have exactly the same properties as the bulk glass.

2.3.2 Planar Resonators: a Key Optical Element for Sensors

An advantage of planar resonators is that they can be miniaturized more than traditional resonators because, even though the planar resonators are small, the light can travel around them multiple times. Miniaturization is important when manufacturing all-integrated microphotonic technology. Planar resonators include micro-disk, micro-ring, and "racetrack" resonators and some examples are shown in Figure 2.8.

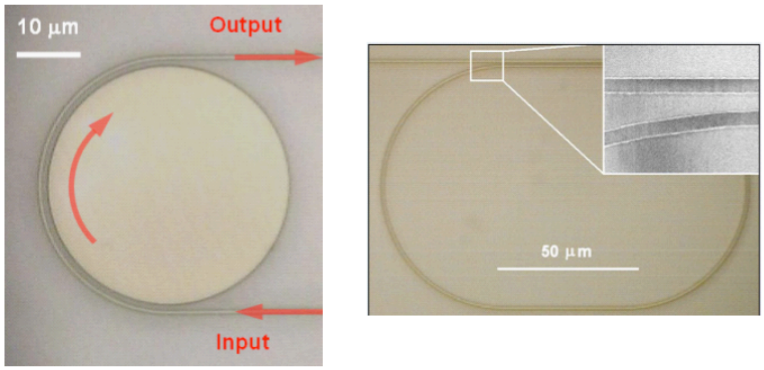

(a) (b)

Figure 2.8: Top view optical micrograph of an As_2S_3 (a) micro-disk resonator with a pulley coupler and (b) a racetrack resonator, taken from reference [7]

With these types of resonators, the light travels through the planar waveguide and then the evanescent wave is coupled into the resonator. The resonator itself is also a sort of waveguide in that it guides the light around it multiple times before it is coupled back into the planar waveguide. The evanescent wave coupling is accomplished by having the planar waveguide very close to, but not touching, the resonator. This can be done in a pulley coupler setup, as shown in Figure 2.8a, or with a straight waveguide next to the resonator, as seen in Figure 2.8b and also illustrated in Figure 2.9.

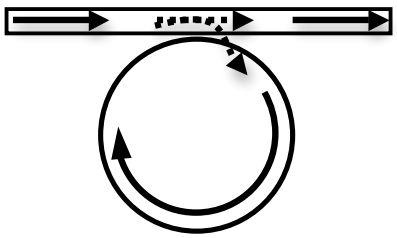

Figure 2.9: Illustration of a micro-disk resonator with a straight waveguide.

With a fiber resonator, the light only travels through it once but with a planar resonator the light can travel around it several times. For this reason, the device can be miniaturized without sacrificing sensitivity by using a planar resonator.

Engineering the surface chemistry of the resonator allows control over how the sensor and the target analyte interact. There are two ways that the sensor can interact with the analyte. The first way is when the analyte is homogeneously distributed in an aqueous medium around the resonator and the second way is that the analyte can adsorb onto the surface of the resonator [26]. The two mechanisms are illustrated in Figure 2.10.

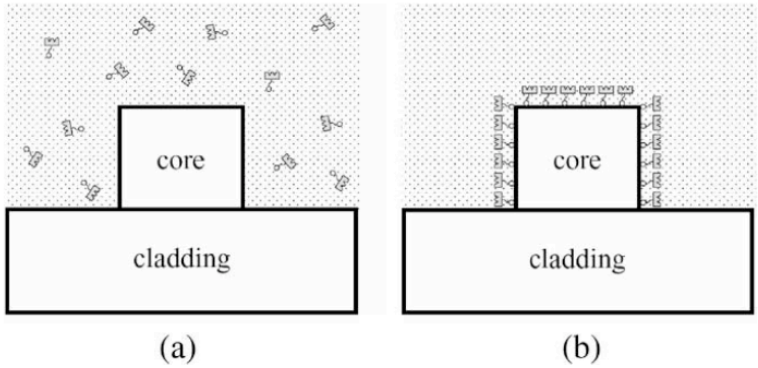

Figure 2.10: Sensing mechanisms. (a) Homogeneous sensing and (b) surface sensing, taken from reference [26]

With homogeneous sensing, the sensor is exposed to not only the target analyte but also other chemicals in the solution/vapor. These other chemicals may have absorptions that interfere with the signal from the target analyte. Surface sensing is more sensitive and selective than homogeneous sensing because the target analyte is bound to the surface so there is less interference from other chemicals [26]. However, the surface needs to be modified in order to allow the analyte to adsorb. Polymers can be grafted to the surface of the resonator in order to bind the target analyte to the surface and improve the sensitivity of the device [7,26]. An example of the improved sensitivity given by having a polymer-coated surface is shown in Figure 2.11. In this experiment, the bare ChG and the polymer-coated ChG were exposed to saturated ammonia vapor.

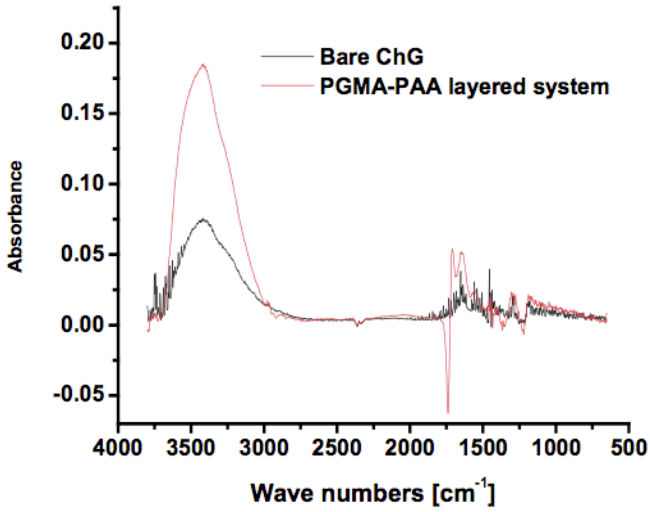

Figure 2.11: FTIR spectra of ammonia vapor over the surface of bare ChG and polymer-coated ChG, taken from reference [7]

As seen in the figure, the polymer coating significantly increases the sensitivity of the sensor by increasing the FTIR absorbance spectra with exposure to the same amount of analyte. Different polymers can be grafted to the ChG surface depending on the target analyte and multiple layers can be deposited for detecting more than one analyte. In this case, a PGMA-PAA layered system was chosen because it was shown to be able to reversibly bind amines [7].

2.4 Focus of this Work

The specific target of this work, in the context of microphotonic chalcogenide sensors, is to investigate and optimize the process of fabricating solution derived thin films of ~800 nm thickness possessing good uniformity and high optical quality. The films should have an index and structure close to that of the parent bulk glass. Ideally, there would be no residual solvent remaining in the film following the heat treatment.

The target attributes of the solution-derived $Ge_{23}Sb_7S_{70}$ thin films are summarized below in Table 2.1.

Table 2.1: Target attributes of solution-derived thin films

Property	**Target Value**
Thickness	~800 nm
Roughness	< 5 nm
Index at 880.7 nm	~2.19
Band gap	~2.61 eV [reference 8]
Residual solvent	None
Surface quality	No pinholes/cracks

2.5 Summary

In this chapter, chalcogenide glasses have been explored as a material to be used in optical biosensors. They have a large transparency window in the infrared region, from 2 μm to as far as 20 μm. This makes them ideal for sensing many molecules that have "fingerprints," or characteristic absorptions, in this region. ChGs can be fabricated as fibers or as thin films, allowing flexibility in the design of sensors. The limitations of fiber sensors, and how planar sensors can overcome these challenges, have been presented. Regardless of the geometry of the sensor, there are several drawbacks to using chalcogenide glasses that must be taken into account. Their toxicity, low glass transition temperature, and low mechanical robustness can make them unsuitable for certain applications.

In order to use ChGs in a lab-on-a-chip device, it is necessary to produce thin films in order to fabricate planar waveguides and resonators. This is far from a simple task because each method of making thin films has its own advantages and disadvantages

that must be considered. The properties of the thin films will never match the properties of the bulk glass exactly, but the goal is to get them as close as possible. Each film fabrication process gives the glass a different thermal history and also induces stresses. This can change the properties even if the composition matches the bulk glass exactly.

Once a high quality thin film has been produced, it can be fabricated into planar waveguides and resonators. Planar micro-ring or micro-disk can increase the sensitivity of an optical biosensor while still allowing miniaturization because the light can travel in a circle around them several times. Modifying the surface of the resonator can also increase the sensitivity. A polymer that can bind to the target analyte can be grafted to the surface of the resonator. The polymer will "grab" the molecules and this will cause them to be concentrated at the surface of the resonator. This increases the sensitivity and also reduces interference from other chemicals in the environment that are not the target analyte.

By using chalcogenide glasses to make planar waveguides and resonators from thin films and then using surface chemistry engineering to modify the surface of the resonator, an optical biosensor can be produced that is sensitive and selective to the target analyte. If a light source and detector can be produced from other materials and put on the same chip as the waveguides and resonator, then an all-integrated "lab-on-a-chip" device can be produced.

2.6 References

1. Rao KJ. *Structural Chemistry of Glasses*. Elsevier Science Ltd: Oxford, UK. p23-26 (2002).
2. Varshneya AK. *Fundamentals of Inorganic Glasses*. Academic Press, Inc: San Diego, CA (1994).

3. Phillips JC. Topology of covalent non-crystalline solids II: medium-range order in chalcogenide alloys and A-Si(Ge). *Journal of Non-Crystalline Solids*. **43**, 37-77 (1981).
4. Thorpe MF. Continuous deformations in random networks. *Journal of Non-Crystalline Solids*. **57**, 355-370 (1983).
5. Lucas J. Infrared glasses. *Current Opinion in Solid State and Materials Science*. **4**, 181-187 (1999).
6. Eggleton BJ, Luther-Davies B and Richardson K. Chalcogenide photonics. *Nature Photonics*. **5**, 141-148 (2011).
7. Richardson K, et al. Progress on the fabrication of on-chip integrated chalcogenide glass (ChG)-based sensors. *Journal of Nonlinear Optical Physics and Materials*. **19**(1), 75-99 (2010).
8. Musgraves JD, et al. Comparison of the optical, thermal and structural properties of Ge-Sb-S thin films deposited using thermal evaporation and pulsed laser deposition techniques. *Acta Materialia*. **59**, 5032-5039 (2011).
9. Sanghera JS, Shaw LB, and Aggarwal ID. Applications of chalcogenide glass optical fibers. *C.R. Chimie*. **5**, 873-883 (2002).
10. Miloshova M, Baltes D, and Bychkov E. New chalcogenide glass chemical sensors for s^{2-} and dissolved H_2S monitoring. *Water Science and Technology*. **47**(2), 135-140 (2003).
11. Zakery A and Elliott SR. Optical properties and applications of chalcogenide glasses: a review. *Journal of Non-Crystalline Solids*. **330**, 1-12 (2003).
12. Popescu MA. *Non-Crystalline Chalcogenides*. Kluwer Academic Publishers: Dordrecht, The Netherlands. p46 (2000).
13. Vlasov YG, Bychkov EA, and Bratov AV. Ion-selective field-effect transistor and chalcogenide glass ion-selective electrode systems for biological investigations and industrial applications. *Analyst*. **119**, 449-454 (1994).
14. Georgieva V, Yordanov TZ, Pamukchieva V, Arsova D, Gadjanova V, and Vergov L. Gas sensing properties of Ge-As-S thin films. *AIP Conference Proceedings*. **1203**, 1079-1084 (2010).
15. Le Coq D, Michel K, Keirsse J, Boussard-Plédel C, Fonteneau G, Bureau B, Le Quéré J-M, Sire O, and Lucas J. Infrared glass fibers for in-situ sensing, chemical and biochemical reactions. *Comptes Rendus Chimie*. **5**, 907-913 (2002).
16. Charpentier F, Bureau B, Troles J, Boussard-Plédel C, Michel-Le Pierrès K, Smektala F, and Adam J-L. Infrared monitoring of underground CO_2 storage using chalcogenide glass fibers. *Optical Materials*. **31**, 496-500 (2009).
17. Márquez E, Bernal-Oliva AM, González-Leal JM, Prieto-Alcón R, and Wagner T. Optical properties and structure of amorphous $(As_{0.33}S_{0.67})_{100-x}Te_x$ and $Ge_xSb_{40-x}S_{60}$ chalcogenide semiconducting alloy films deposited by vacuum thermal evaporation. *Journal of Physics D: Applied Physics*. **39**, 1793-1799 (2006).
18. Rode AV, Zakery A, Samoc M, Charters RB, Gamaly EG, and Luther-Davies B. Laser-deposited As_2S_3 chalcogenide films for waveguide applications. *Applied Surface Science*. **197-198**, 481-485 (2002).

19. Frumar M, Frumarova B, Nemec P, Wagner T, Jedelsky J, and Hrdlicka M. Thin chalcogenide films prepared by pulsed laser deposition – new amorphous materials applicable in optoelectronics and chemical sensors. *Journal of Non-Crystalline Solids*. **352**, 544-561 (2006).
20. Choy KL. Chemical vapour deposition of coatings. *Progress in Materials Science*. **48**, 47-170 (2003).
21. Huang CC, Wu CC, Knight K, and Hewak DW. Optical properties of CVD grown amorphous Ge-Sb-S thin films. *Journal of Non-Crystalline Solids*. **356**, 281-285 (2010).
22. Wasa K, Kitabatake M, and Adachi H. *Thin Film Technology: Sputtering of Compound Materials*. William Andrew, Inc: Norwich, NY. P39-40 (2004).
23. Frantz JA, Sanghera JS, Shaw LB, Villalobos G, Aggarwal ID, and Hewak DW. Sputtered films of Er^{3+}-doped gallium lanthanum sulfide glass. *Materials Letters*. **60**, 1350-1353 (2006).
24. Chern GC and Lauks I. Spin-coated amorphous chalcogenide films. *Journal of Applied Physics*. **53**(10), 6979-6982 (1982).
25. Song S, Carlie N, Boudies J, Petit L, Richardson K, and Arnold CB. Spin-coating of $Ge_{23}Sb_7S_{70}$ chalcogenide glass thin films. *Journal of Non-Crystalline Solids*. **355**, 2272-2278 (2009).
26. Chao C-Y and Guo LJ. Design and optimization of microring resonators in biochemical sensing applications. *Journal of Lightwave Technology*. **24**(3), 1395-1402 (2006).

CHAPTER THREE

EXPERIMENTAL METHODS

In this chapter, the methods used to fabricate bulk glass and deposit solution-derived films will be described. The techniques for characterizing the structure and optical and physical properties of bulk and thin film samples will also be discussed in detail. This includes the development of in-situ measurement methods to track changes in film properties during heat treatment using infrared and UV-vis spectroscopy.

3.1 Sample Preparation

In order to fabricate the thin films that are the focus of this study, bulk glass was made by batching and melting elemental materials. High purity starting materials were used and no extra purification was performed on the materials. Batching of starting materials and film deposition were performed in nitrogen-purged glove boxes in order to avoid the presence of impurities such as oxygen and hydrogen, which absorb in the infrared region.

3.1.1 Bulk Glass

The first step in preparing bulk chalcogenide glass is batching. This is done in a nitrogen-purged glove box. Appropriate amounts of each starting material are weighed and placed in a fused silica ampoule. The ampoule containing the batch is then placed under vacuum while being heated at 90°C. Heating the batch during vacuuming helps drive off any water that might be on the ampoule or the starting materials. However, the temperature must be low enough to avoid volatilization of the materials, particularly sulfur. Next, the ampoule is sealed. This is done using a methane-oxygen torch after the

ampoule has been under vacuum for approximately 4 hours. The sealed ampoule is placed into a rocking furnace and heated to the melting temperature at a rate of 2.5 °C/min. Melting temperatures range from 650-925 °C, depending on the glass composition, with holding times at this temperature ranging from 12-24 hours depending on the mass of the batch. The rocking furnace ensures homogenization of the batch during melting. For the last 10 minutes of the melting process, the rocking of the furnace is stopped so that the ampoule is resting in a vertical position and the temperature is decreased by about 25-50 °C. This allows any bubbles in the melt to rise to the top rather than being trapped in the melt. Quenching is performed by removing the ampoule containing the melt from the furnace and allowing it to cool in air at room temperature. Samples are annealed overnight at 40°C below the T_g.

3.1.2 Solution-Derived Films

After the bulk glass has been fabricated, it is crushed into a fine powder using a mortar and pestle. The glass can be crushed in air, but subsequent steps were performed in a nitrogen atmosphere. Sources of error in this step include the possibility of introducing impurities into the glass from the mortar and pestle or from the atmosphere during crushing.

For films deposited at *Clemson University*, a programmable computer-controlled spin-coater (Model G3 from Specialty Coating Systems) was used to deposit the films following dissolution. During spin coating, four variables can be controlled: acceleration time (time to reach spin speed), spin speed, spin time, and deceleration time (time to reach 0 rpm from the spin speed). These variables can affect the thickness and roughness

of the resulting films. Films were deposited on both silicon and borosilicate substrates in order to be able to fully characterize them.

For films deposited at the *University of Bordeaux 1*, all efforts were made to maintain uniformity to materials prepared at Clemson. A new facility was built to allow this to be done, as shown in Figure 3.1. The glove box was purged with nitrogen containing < 3 ppm of water and < 2 ppm of O_2 and maintained at a temperature of 22-23°C. Shown also is a model SCI-20 spin-coater from Novocontrol Technologies which was used for depositing the films. The only variable that can be controlled on this device is the spin speed. The acceleration and deceleration cannot be changed and the spin time must be controlled manually. The acceleration rate can affect film thickness, so films made in Bordeaux with the same spin speed as films made in Clemson were thinner due to a higher acceleration rate. This will be discussed in Chapter 5. All spin parameters besides acceleration rate were kept constant for films deposited at both universities.

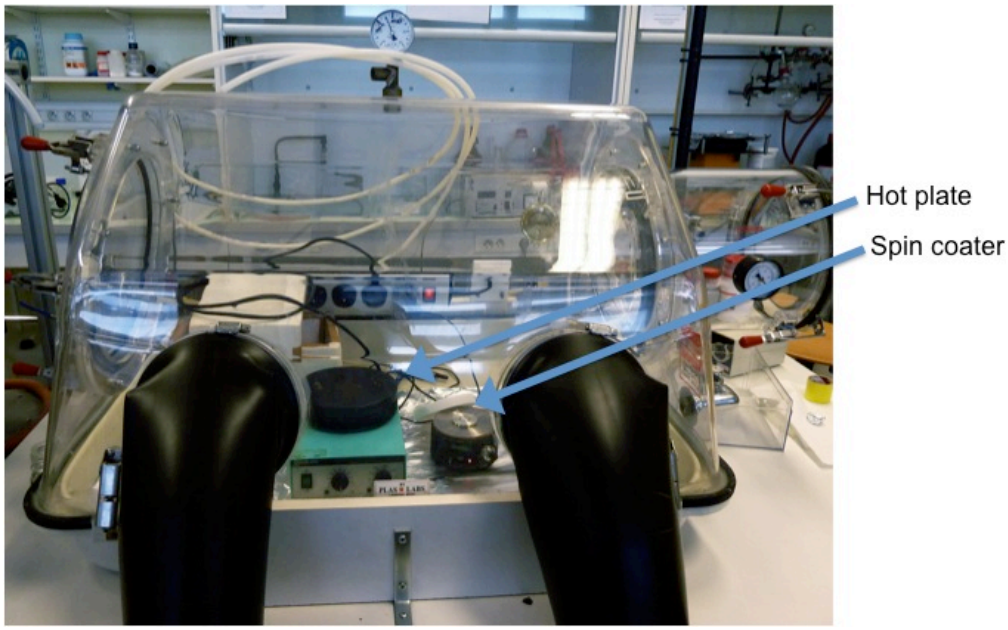

Figure 3.1: Facility for depositing solution-derived films. Shown is the glove box containing a hot plate and spin coater.

The solvent used was propylamine and it was prepared by drying it overnight with a molecular sieve. Then the glass solution was made by adding a specific amount of deionized water to 10 mL of dried propylamine and 0.2-0.9 g of glass powder. The amount of water added to the propylamine ranged from 26-36 μL, depending on glass composition and solution concentration. The solution was stirred at room temperature until completely dissolved, usually overnight. The final step is heat treatment to drive off residual solvent. A two-step process was used. Immediately after deposition, the soft bake is performed by placing the film on a hot plate at ~50 °C for 3-4 minutes in nitrogen atmosphere. The soft bake drives off some of the solvent and solidifies the film enough to be removed from the inert atmosphere and transferred to another furnace for the hard bake. The films were hard baked under vacuum at *Clemson University* and under dry air atmosphere at the *University of Bordeaux 1*. While an inert atmosphere is preferable, dry

air was the only option available for the heat treatments in Bordeaux. The absorptions due to oxide impurities are outside the range of interest (3-3.5 μm), but water impurities absorb in this range so dry air is suitable for the heat treatments. The hard bake is aimed at removing any remaining solvent and completely densifying the film. Experiments were performed to determine the effect of varying the time and temperature of the hard bake and the results will be discussed in detail later.

3.2 Materials Characterization

The physical, optical, and structural properties of the bulk and thin film materials were characterized using a variety of techniques. These techniques included white light interferometry, scanning electron microscopy (SEM) with electron dispersive spectroscopy (EDS), ellipsometry, UV-visible spectroscopy, Raman spectroscopy, and Fourier transform infrared spectroscopy (FTIR).

3.2.1 Physical Properties

The thickness and roughness of the solution-derived thin films was determined using a Zygo (NewView 6300) white-light interferometric microscope. In order to measure thickness, a small area of the film was scratched off, leaving bare substrate. Then the two areas were compared to determine the film thickness. Roughness and thickness were measured in at least 5 areas across the surface of the film and the average and standard deviation were calculated.

Atomic force microscopy (AFM) was performed using an Agilent Technologies (Model 5500) AFM to inspect the topography and roughness of the surface of the films. The tip used was a Nanosensor PPP-FMR. This technique was first described in [1] and

involves scanning the surface of the sample using a cantilever beam with a sharp tip on the end. The tip is brought in close proximity to the surface of the sample and the cantilever is deflected due to forces between the sample and the tip. To measure the deflection, a laser beam is reflected off of the back of the cantilever and the angle of reflection is measured. Throughout the scan, the height of the beam (in the z direction) is adjusted in order to maintain the same angle of reflection of the laser beam. This keeps the force of the tip on the sample constant in order to prevent damage to the tip or the sample. Following the scan, the topography of the surface can be imaged by plotting the height, z, as a function of x and y. The results can be analyzed to determine roughness as well as the dimensions of various features (bubbles, holes, etc) on the surface of the sample.

3.2.2 Optical Properties

The refractive index and dispersion of the bulk glass and solution-derived films was measured using a Nanofilm Surface Analysis ellipsometer and applying the Cauchy dispersion model using the system's software (EP4_Model). The index was measured at several wavelengths from 630.7-1001.7 nm in order to plot a dispersion curve. The principles of ellipsometry are described in detail in [2]. An ellipsometer consists of a light source, a polarizer, optical compensators, an analyzer a detector, as seen in Figure 3.1 below. The angle of incidence is equal to the angle of reflection.

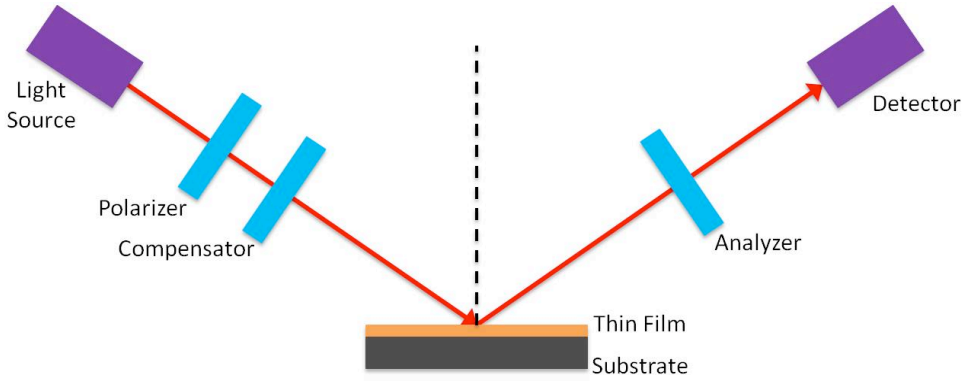

Figure 3.2: Illustration of the setup of an ellipsometry measurement

Ellipsometry is based on the principle that the polarization of light changes after it is reflected off of the surface of a material. Rather than being defined by an x-y coordinate system, the polarization state of light is defined by its p (parallel) and s (perpendicular) components. First, the source light is emitted and is polarized. Then it may pass through an optical compensator, such as a quarter-wave plate, which can change the polarization. The light reflects off of the surface, passes through the analyzer, which is a polarizer, and is collected by the detector. The detector measures the amplitude of the s and p components of the polarization of the reflected light, which are then normalized to their initial values. These values are the complex reflection coefficients and can be denoted as r_p and r_s. The ratio of the complex reflection coefficients, ρ, is defined as shown in equation 3.1 below:

$$\rho = \frac{r_p}{r_s} = \tan(\Psi)e^{i\Delta} \qquad (3.1)$$

where Δ and tan(ψ) are the phase shift and the ratio of amplitude change, respectively, of the p and s components after reflection. An optical model, such as the Cauchy dispersion

law, can be applied to determine the dispersion curves and the thickness of the film after these measurements have been made at multiple wavelengths. The complex refractive index of the substrate must be incorporated into the model.

The UV-visible absorption spectra of the bulk glass and films were measured using a Varian Cary 5000 UV-Visible-NIR spectrometer. A double-beam configuration was used. These spectra allowed the comparison of the absorption edge of the bulk glass and films. It is possible to calculate the optical band gap from the absorption spectra of the films. The high absorption region ($\alpha > 10^4$ cm^{-1}) of the spectra can be described by the Tauc power law [3]:

$$\alpha h\nu = B\left(h\nu - E_g\right)^2 \qquad (3.2)$$

where α is the absorption coefficient, hv is the photon energy, B is the slope of the Tauc edge, and E_g is the optical band gap energy. The optical band gap can be determined by plotting $(\alpha h\nu)^{1/2}$ vs $h\nu$, extending the linear section of the curve to the x-axis, and finding the x-intercept.

3.2.3 Structural Properties

The main technique used to characterize the structure of the bulk glass and thin films was Fourier transform infrared spectroscopy in the mid- and far-IR regions. Spectra were recorded under vacuum using a Bruker model Vertex 70v FTIR spectrometer. FTIR can be used to identify absorptions due to bonds in the glass network (far-IR) as well as impurities, such as oxides and hydroxides (mid-IR). Absorptions due to residual solvent and glass-solvent interactions in the spin-coated films can also be identified in the mid-IR region. For the bulk glass, a reflection spectrum was measured and a Kramers-Kronig

transformation was performed to determine the real, *n*, and imaginary, *k*, components of the complex refractive index. Then, the absorption coefficient can be calculated according to equation 3.3 below:

$$\alpha = 4\pi k\nu \qquad (3.3)$$

where *v* is the frequency in cm^{-1}. By using this method, the absorption coefficient can be plotted vs. wavenumber and the absorptions of the glass network can be identified. This is not possible through transmission IR measurements with bulk glass due to saturation of the absorption.

For thin films, transmission IR spectra can be used directly to characterize the structure. However, optical interference due to reflections at the multiple interfaces must be accounted for in the analysis of the spectra. The interference varies with film thickness and refractive index and depends on the substrate as well as the glass thin film. In order to investigate the role of optical interference on the IR spectra of thin films, an optical model was used to simulate the IR spectra of films of various thicknesses using the *n* and *k* data obtained from the bulk glass. The optical model will be described in detail in Chapter 6.

Raman spectroscopy is another technique that was used to characterize the structure of the bulk glass. A good Raman signal could not be obtained on the thin films due to their low thicknesses. The principles of Raman spectroscopy are described in [4]. The sample is irradiated with a single wavelength of light, which interacts with the molecules and is scattered. Raman scattering is caused by nuclear motion of the molecule and is an inelastic process, so the energy of the scattered photon differs from that of the

incident photon. This energy difference is measured and can be assigned to vibrational energies of chemical bonds in the material. Raman scattering usually has a low intensity and requires the use of a light source with a high intensity. Chalcogenides can be photosensitive [5] and care should be taken to ensure that the glass structure is not modified during the measurements. For the bulk glass and thin films, a 752 nm laser and a 632 nm laser were used as the excitation sources, respectively. The reason for using a higher energy laser for the thin films was to attempt to obtain a higher signal.

FTIR and Raman spectroscopy are complementary techniques that can give different information about the structure of a material. Asymmetric vibrations give the more intense absorptions in FTIR spectroscopy while symmetric vibrations cause the most scattering and the largest energy changes [4].

3.3 In-Situ Infrared (IR) Spectroscopy Measurements

To track the removal of solvent over time during the heat treatment process, an in-situ IR measurement process was developed for as-formed glass films, and their subsequent step-wise solvent evolution, within a dry air atmosphere. In the measurement, a background spectrum was collected with the empty furnace/sample holder set-up. Then the film was placed in the furnace and the sample holder was assembled, as shown in Figure 3.2 below.

a) b)

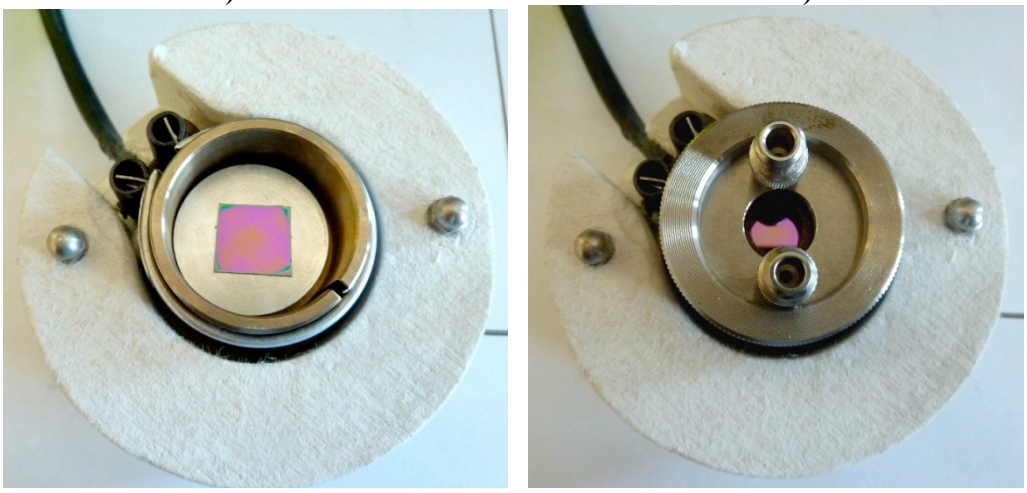

Figure 3.3: Furnace used for in-situ IR measurements of thin films (a) before and (b) after assembling sample holder. Shown is a ChG film coated-Si wafer inserted in the furnace which will then be inserted into the FTIR.

The furnace was then placed into the FTIR spectrometer and the lid was closed as much as possible as shown in Figure 3.3.

a) b)

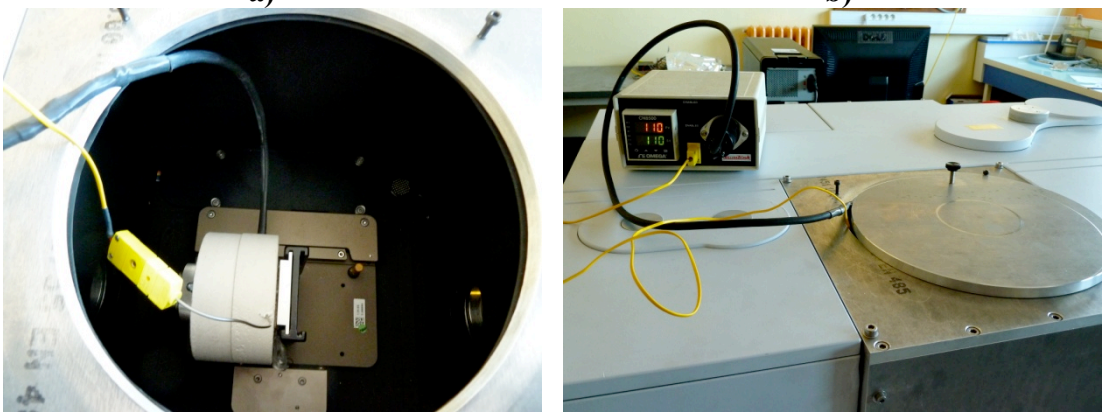

Figure 3.4: (a) In-situ furnace placed in FTIR spectrometer. (b) Sample chamber lid is closed as much as possible while still allowing thermocouple and power cord to be plugged in.

The sample chamber was continuously purged with dry air during the measurements and a spectrum was collected every 5 minutes. By allowing measurements

to be made throughout the heat treatment rather than only before and after, this set-up enabled a determination of the kinetics of solvent removal from the glass films. It also permitted the tracking of changes in the structure of the glass film and the nature of the glass-solvent interactions during the heat treatment.

In-situ UV-Vis absorption measurements were performed in the same way. These measurements allowed the determination of the kinetics of the shift in the cutoff wavelength. The changes in the bandgap of the glass with heat treatment temperature could also be estimated.

3.4 Summary

In this chapter, the experimental methods for fabrication of bulk glass and solution derived films were presented. Differences between film deposition and processing conditions between Clemson University and the University of Bordeaux 1 were highlighted. The differences in fabrication parameters, particularly the acceleration rate during spin-coating, may lead to variations in the properties of the post-processed films. This was taken into account and the impact of the acceleration rate will be discussed in Chapter 5. The techniques used to characterize the physical, optical, and structural properties of the bulk and thin film samples were described. In-situ measurement techniques were developed for this study and a description of these methods was presented.

3.5 References

1. Hu J, Carlie N, Feng N-N, Petit L, Agarwal A, Richardson K, and Kimerling L. Planar waveguide-coupled, high-index-contrast, high-Q resonators in chalcogenide glass for sensing. *Optics Letters*. **33**(21), 2500-2502 (2008).

2. Imaging Ellipsometry – Principles of Operation for Surface Characterization http://www.azonano.com/article.aspx?ArticleID=2944
3. Tauc J and Menth A. States in the gap. *Journal of Non-Crystalline Solids*. **8-10**, 569-585 (1972).
4. Smith E and Dent G. *Modern Raman Spectroscopy: A Practical Approach*. John Wiley & Sons, Ltd: Chichester, England (2005).
5. Zakery A and Elliott SR. Optical properties and applications of chalcogenide glasses: a review. *Journal of Non-Crystalline Solids*. **330**, 1-12 (2003).

CHAPTER FOUR

CHARACTERIZATION OF BULK GLASS AND THERMALLY EVAPORATED (TE) FILM REFERENCE MATERIALS

In this chapter, the structure and optical properties, including the transmission window and refractive index, of bulk $Ge_{23}Sb_7S_{70}$ and $Ge_{23}Sb_4S_{73}$ are discussed. Characterization of the bulk glass is important because it is the reference material for the thin film studies. Ideally, the fabricated thin films would have a structure and optical properties matching that of the bulk. Glasses in the Ge-Sb-S family have been the subject of many studies and their properties are well known [1-2]. $Ge_{23}Sb_7S_{70}$ was chosen because it has previously been demonstrated in thermally evaporated form [3-4], which can be used as a basis for comparison in this study. It has also been demonstrated as a suitable composition for spin-coated films [5] and is transparent in the infrared, including the 3-3.5 μm region of the light source. $Ge_{23}Sb_4S_{73}$ was chosen to explore the effects compositional changes on glass dissolution and thin film deposition.

4.1 Bulk Glass: Optical Properties

To be able to compare the optical properties of thin films derived from bulk ChG materials, it is necessary to quantify these attributes, which will serve as the target goal of our study. Recall that one of the defined objectives of the work is to realize solution-derived ChG films that have physical properties identical to its parent bulk material. The UV-Vis-NIR and FTIR absorption spectra for $Ge_{23}Sb_7S_{70}$ and $Ge_{23}Sb_4S_{73}$ are shown in Figure 4.1 below. The FTIR transmission spectra of bulk $Ge_{23}Sb_7S_{70}$ and $Ge_{23}Sb_4S_{73}$

were converted to absorbance and then normalized to the thickness in order to plot the absorption coefficient.

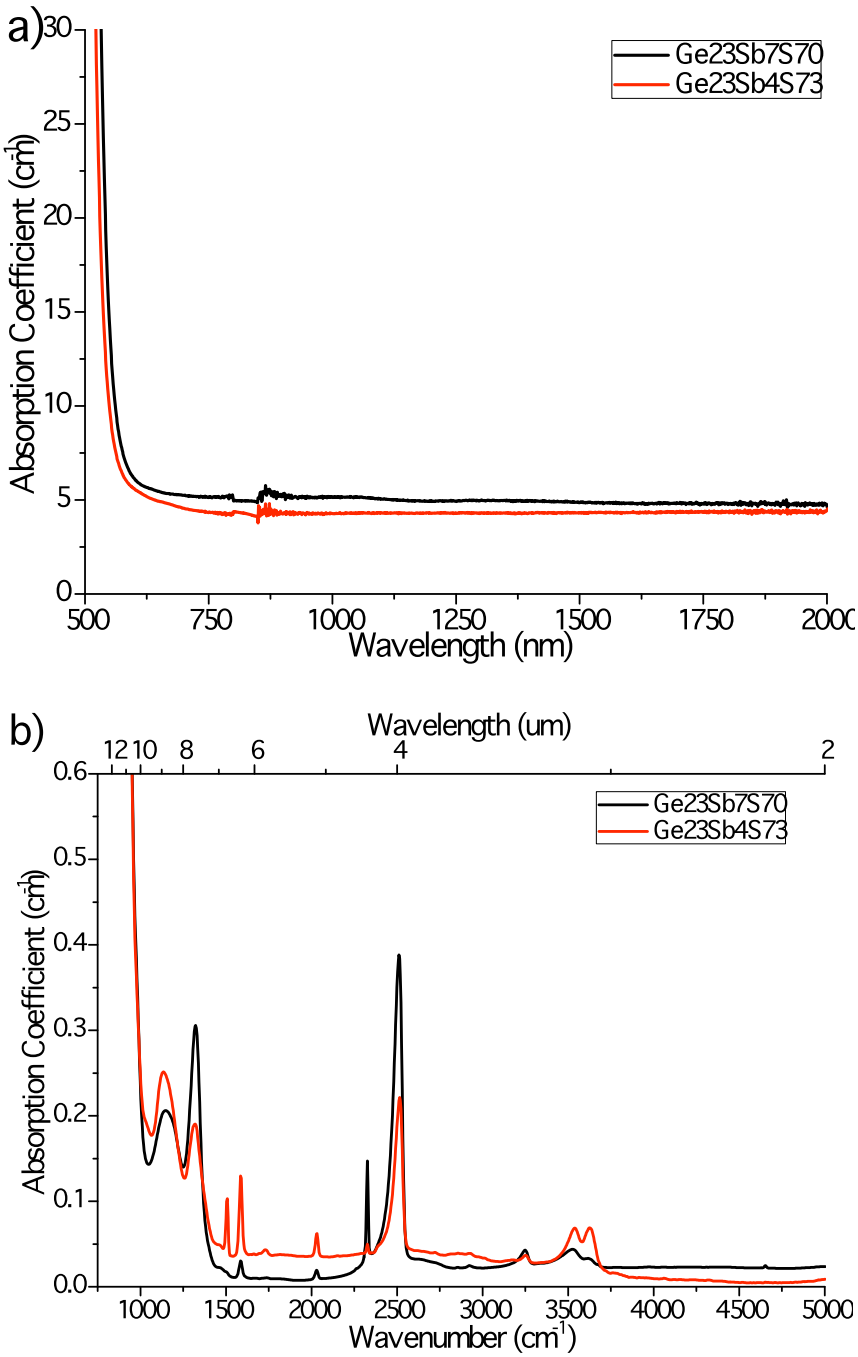

Figure 4.1: (a) UV-Vis-NIR and (b) FTIR absorption spectra for bulk $Ge_{23}Sb_7S_{70}$ and $Ge_{23}Sb_4S_{73}$.

From these spectra, the transmission window of the glasses can be determined. As seen the Figure 4.1a, these glasses are transparent throughout the near-IR region. There is a small shift of the cutoff wavelength toward the near-IR with higher antimony content. This is consistent with previous results [1]. Figure 4.1b shows that the glasses are also transparent throughout most of the mid-IR except for small impurity absorptions. Based on this data, both compositions are transparent from approximately 520 nm to 10.5 μm. This makes them suitable materials for use in a chemical sensor with a source wavelength of 3-3.5 μm.

Besides determining the transmission window, the IR spectra in Figure 4.1b can be used to identify impurities in the glasses. Hydrogen impurities cause an absorption band at 2500 cm^{-1} due to S-H stretching and the peak near 1600 cm^{-1} can be attributed to H_2O impurities [6]. Broad absorptions near 3500 cm^{-1} are related to impurities from water, either as interstitial H_2O or as –OH impurities in the glass network, such as Ge-OH. At this time it is unclear what impurities are specifically causing the absorption seen in these glasses between 1100 and 1300 cm^{-1}. However, as previous studies have shown absorptions due to Ge-O impurities at approximately 1260 cm^{-1} [7], it is likely that they arise from oxygen impurities on the metal cations (Ge and/or Sb). While there are some minor differences between the two compositions, all of the impurity absorptions are small. The absorptions from water are in the 3-3.5 μm region of the proposed source wavelength, so purification of the glass to remove these impurities prior to film deposition could reduce loss in the sensor.

The refractive index of the bulk glasses was measured using ellipsometry and the dispersion curves are shown in Figure 4.2 for the region of 630-880 nm.

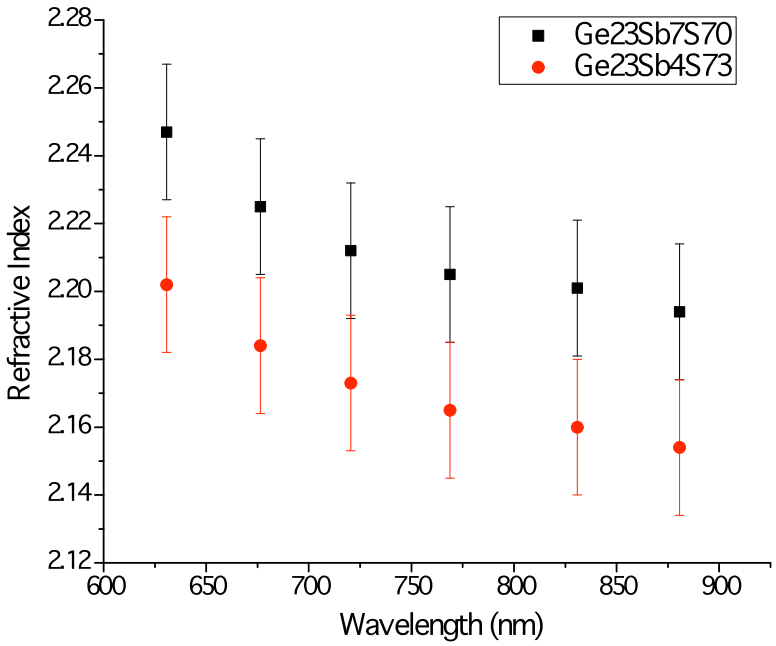

Figure 4.2: Visible and infrared refractive index data for bulk $Ge_{23}Sb_7S_{70}$ and $Ge_{23}Sb_4S_{73}$.

It is clear from the figure that the refractive index is higher for the $Ge_{23}Sb_7S_{70}$. These results are in agreement with previous studies that show an increase in the refractive index of Ge-Sb-S glasses as the antimony content increases [1]. Pure germanium sulfide glass is composed of GeS_4 tetrahedra. When antimony is added, it forms SbS_3 trigonal pyramids, which contain a lone pair of electrons. Antimony also has more outer shell electrons than germanium and sulfur. The outer shell electrons and the lone pairs enhance the polarizability of the glass, which is directly linked to the refractive index [8-9].

4.2 Bulk Glass: Structural Characterization

The structure of the bulk glasses was investigated using FTIR spectroscopy and Raman spectroscopy. To analyze the structure of the glass network using FTIR, reflection spectra were measured and analyzed in order to calculate an absorption spectrum. The complex refractive index of the bulk glasses was obtained through performing a Kramers-Kronig (KK) transformation on their measured far-IR reflectance spectra as described in [10]. In this way, most of the absorptions from impurities are not considered in the calculations. The far-IR reflection spectra and the calculated real, n, and imaginary, k, parts of the refractive index for bulk $Ge_{23}Sb_7S_{70}$ and $Ge_{23}Sb_4S_{73}$ are shown below in Figure 4.3.

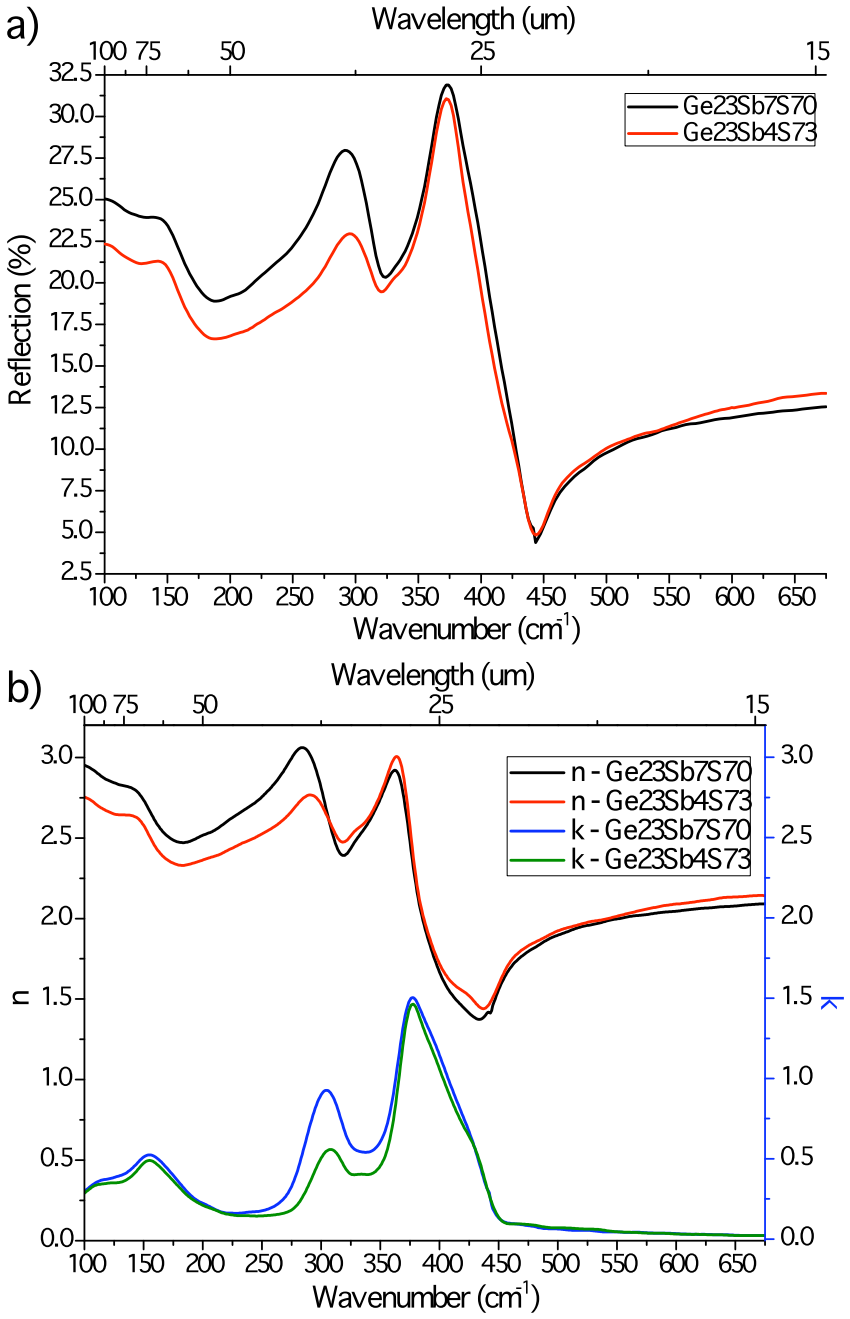

Figure 4.3: Detailed view of the far-IR (a) reflection spectra and (b) calculated real, *n*, and imaginary, *k*, parts of the complex refractive index for bulk $Ge_{23}Sb_7S_{70}$ and $Ge_{23}Sb_4S_{73}$.

Using the complex refractive index data presented in Figure 4.3, the absorption

coefficient, α, can be calculated using Equation 4.1 shown below.

$$\alpha = 4\pi k\nu \qquad (4.1)$$

In this equation, ν is the frequency in cm^{-1} and k is the imaginary part of the complex refractive index calculated using the KK transformation. The results are shown below in Figure 4.4

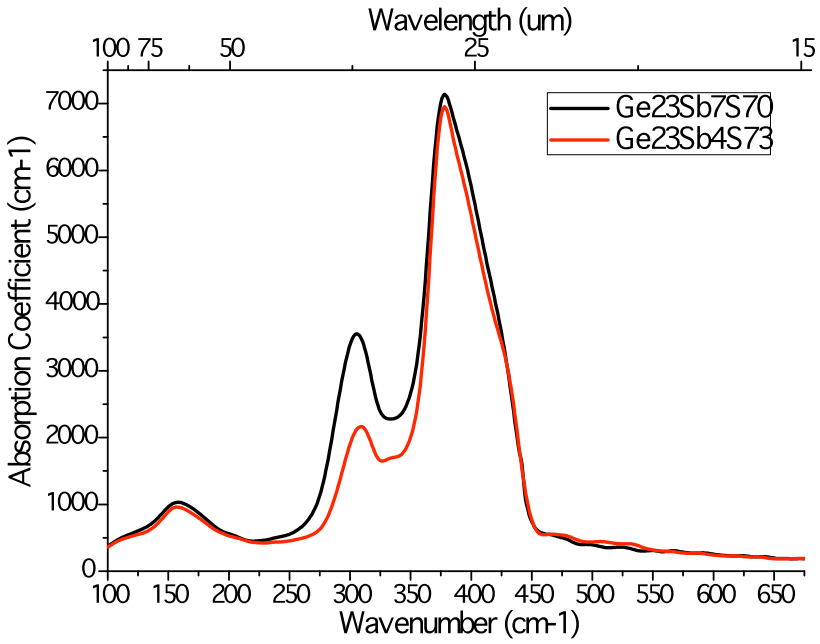

Figure 4.4: Calculated absorption coefficient for bulk $Ge_{23}Sb_7S_{70}$ and $Ge_{23}Sb_4S_{73}$.

The main absorption peaks are the asymmetric stretching mode of GeS_4 tetrahedral units around 370 cm^{-1} and the asymmetric stretching mode of SbS_3 trigonal pyramids at 290-300 cm^{-1} [1,11]. As expected, the peak due to SbS_3 stretching increases for a higher antimony content. The small shoulder near 430 cm^{-1} is due to vibration of

tetrahedral units that are linked by S-S bridges [11]. The third peak, located at approximately 150-160 cm^{-1} is linked to the bending mode of GeS_4 tetrahedra [1,11]. A summary of the IR absorption peaks can be found in Table 4.1 below.

Table 4.1: Summary of far-IR absorption bands of bulk Ge-Sb-S glasses

Absorption Band (cm^{-1})	**Assignment**	**Reference**
150-160	Bending mode of GeS_4 tetrahedra	[1,11]
290-300	Asymmetric stretching mode of SbS_3 trigonal pyramids	[1,11]
370	Asymmetric stretching of GeS_4 tetrahedra	[1,11]
430	Vibration of GeS_4 tetrahedral units linked by S-S bridges	[11]

Raman spectroscopy is another technique used to characterize the structure of the bulk glasses. The Raman spectra of bulk $Ge_{23}Sb_7S_{70}$ and $Ge_{23}Sb_4S_{73}$ are presented in Figure 4.5 below.

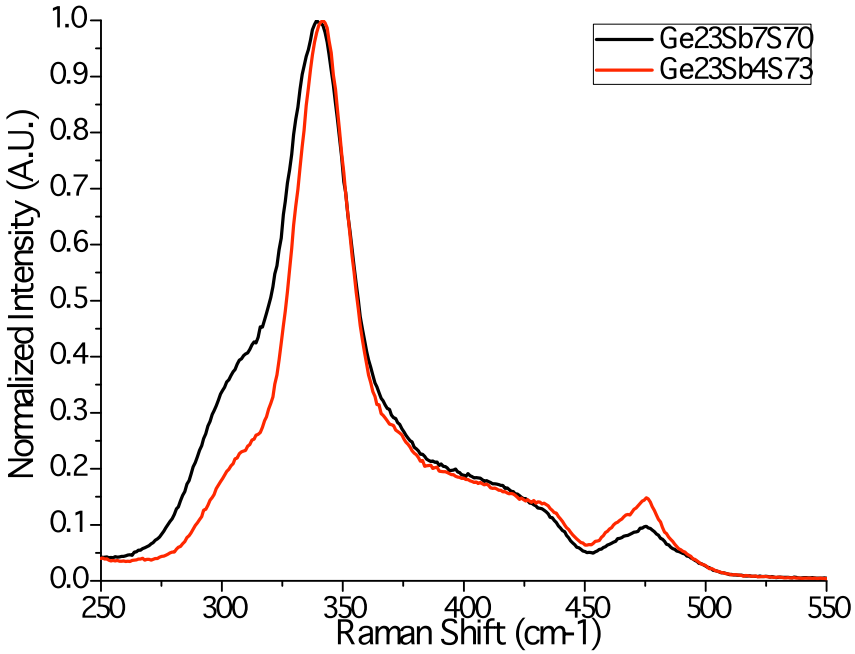

Figure 4.5: Raman spectra of bulk $Ge_{23}Sb_7S_{70}$ and $Ge_{23}Sb_4S_{73}$

A detailed description of the Raman spectra of Ge-Sb-S glasses can also be found elsewhere [12]. The main peak centered near 340 cm^{-1} is attributed to the symmetric stretching mode of GeS_4 tetrahedral units [11-12]. The main band has a shoulder at higher wavenumbers, which can be assigned to edge-shared $Ge_2S_2S_{4/2}$ bi-tetrahedra, asymmetric stretching of GeS_4 units, and stretching of $S_{3/2}Ge\text{-}S\text{-}GeS_{3/2}$ bridges at 370, 400, and 425 cm^{-1}, respectively [3]. The shoulder near 290-300 cm^{-1} is due to the presence of $SbS_{3/2}$ trigonal pyramids [11-12] and increases with increasing antimony content. The slight shift to lower wavenumbers and broadening of the main peak has also been linked to an increase in $SbS_{3/2}$ units [12]. The peak located at approximately 470-475 cm^{-1} is due to the vibration mode of S_8 rings in the glass network [12]. This peak is larger for $Ge_{23}Sb_4S_{73}$ because this glass has a higher sulfur content. A summary of the Raman peaks can be found below in Table 4.2.

Table 4.2: Summary of Raman band assignments of bulk Ge-Sb-S glasses

Raman Shift (cm^{-1})	Assignment	Reference
290-300	$SbS_{3/2}$ trigonal pyramids	[11-12]
340	Symmetric stretching of GeS_4 tetrahedra	[11-12]
370	Edge-shared $Ge_2S_2S_{4/2}$ bi-tetrahedra	[3]
400	Asymmetric stretching of GeS_4 tetrahedra	[3]
425	Stretching of $S_{3/2}Ge$-S-$GeS_{3/2}$ bridges	[3]
470-475	Vibration of S_8 rings	[12]

The properties of the bulk glass will be used as target goals for the properties of the solution-derived films discussed in future chapters. However, film deposition processes cause some of the properties to change. Since thermally evaporated films have been successfully incorporated into chemical sensors in our group, they will be used as another point of reference. The properties of these films are described in the following section.

4.3 Properties of TE Films

The properties of TE films have been studied in detail in references [3] and [13]. Some of the properties were also measured over the course of the current study. Shown in Table 4.3 is a comparison of several of the key optical and physical properties important to the present study, for bulk $Ge_{23}Sb_7S_{70}$ glass and thin films produced by thermal evaporation.

Table 4.3: Summary of the properties of annealed TE $Ge_{23}Sb_7S_{70}$ films

Property	Value	Reference
Band Gap	2.54 eV (as-deposited) 2.61 eV (annealed)	[3]
Refractive index at 850 nm	2.21	[3]
Roughness	1.6 ± 0.3 nm	[13]
Transmission Loss at 1550 nm	2.3 dB/cm	[4]

The refractive index is slightly higher than that of the bulk glass, which is believed to be due to mid-gap states formed by bonding defects [3]. The bond defects are present because of the rapid quench rate experienced by the films. Roughness can cause optical loss in the films, so it should be minimized as much as possible. For TE films, one way to reduce the optical loss is to use a method known as "thermal reflow" to reduce sidewall roughness. Thermal reflow involves heating the films to > 50°C above the glass transition temperature for approximately 15 s and then quenching and the surface tension causes a smoothing of the surface [14]. This can be done for blanket (flat) thin films or for waveguides. The transmission loss is important because it determines the number of times that the source light can travel around the resonator, which influences the sensitivity (as discussed in Chapter 2).

The optical band gap of the TE film was estimated by constructing a Tauc plot from UV-Vis absorption data. The method for making a Tauc plot for thin films was described in Chapter 3. The UV-Vis absorption spectrum and tauc plot for an as-deposited $Ge_{23}Sb_7S_{70}$ TE film are shown in Figure 4.6 below.

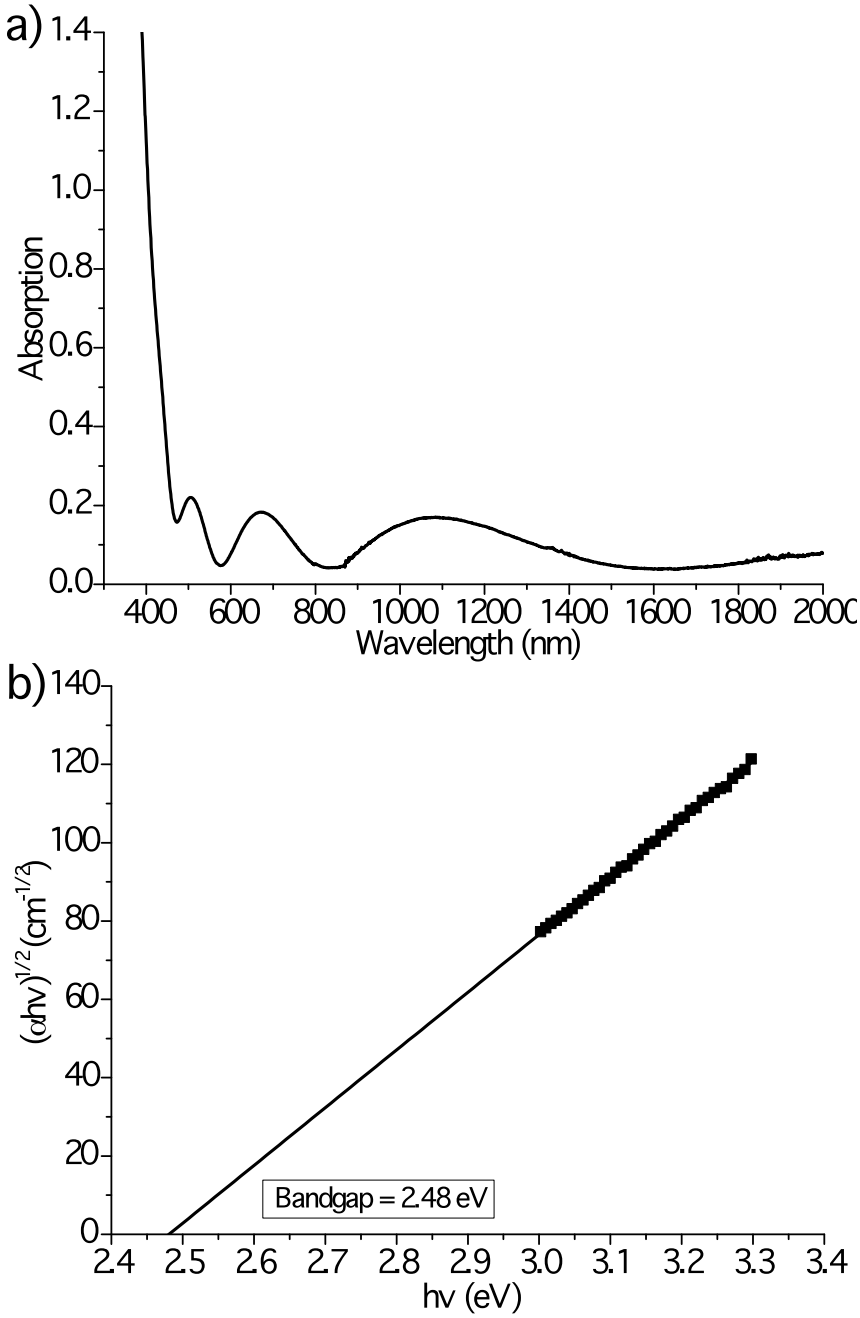

Figure 4.6: (a) UV-Vis absorption spectrum and (b) calculated Tauc plot of an as-deposited $Ge_{23}Sb_7S_{70}$ TE film.

In Figure 4.6a, the fringes seen in the spectrum are from optical interference due to reflections at the multiple interfaces. The data at lower wavelengths where there was

no optical interference was used to calculate the Tauc plot. The optical band gap was found by performing a linear curve fit on the linear section of the curve in Figure 4.6b. Then, the linear curve fit was extrapolated to find the x-intercept. For this film, the band gap was found to be 2.48 eV, which is a little lower than the value of 2.54 eV reported for an as-deposited film in the literature [3]. The band gap has been shown to increase when the film is annealed [3]. The film should be annealed to determine if the band gap increases to the reported value of 2.61 eV [3] for an annealed film.

In the study in reference [3], the Raman spectra of TE films showed that the main peak was shifted to lower wavenumber compared to the bulk glass spectrum. The Raman spectra also showed that there was a decrease in the intensity of the peak, indicating a reduction of sulfur rings. However, the appearance of a band at 250 cm^{-1} indicated the presence of homopolar Ge-Ge bonds. The appearance of these bonds, which are thermodynamically unfavorable, is believed to be due to the rapid quenching of the film compared to the bulk glass. These homopolar Ge-Ge bonds are not desired in the solution-derived films.

For the current study, the main tool to investigate the glass structure in thin films is IR spectroscopy. However, the IR spectra of thin films must be considered carefully because the shape and position of absorption peaks can change due to optical interference as well as changes in the glass composition and structure. It is necessary to predict the spectral changes induced by optical effects. An optical model, described in detail in [10], was used to predict the transmission IR spectrum for an "ideal" film whose properties match those of the bulk glass. The optical properties of the bulk glass and the silicon

substrate need to be accounted for in the model. Figure 4.7 shows a schematic diagram of how light propagates through a bilayer system.

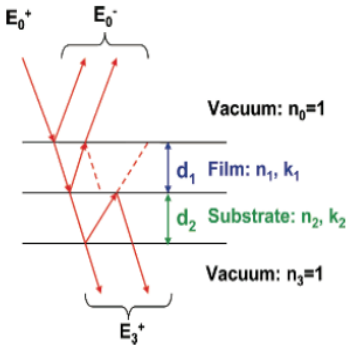

Figure 4.7: Diagram of how light propagates through a bilayer film/substrate system, taken from reference [10]

Thus, the inputs of the model are: (1) the optical constants of the reference bulk glass, (2) the optical constants of the substrate and (3) the thicknesses of the film and the substrate. The only parameter that will be varied in the model is the film thickness. The calculated spectra for the real, *n*, and imaginary, *k*, parts of the refractive index for the bulk $Ge_{23}Sb_7S_{70}$ glass and the silicon substrate are shown below in Figure 4.8.

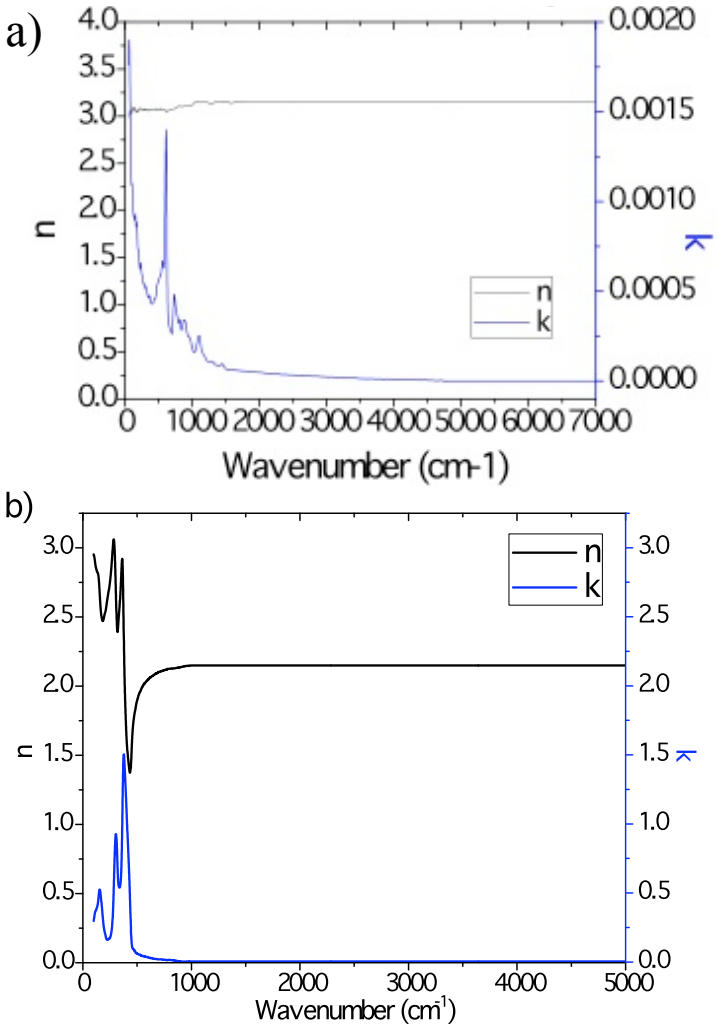

Figure 4.8: Calculated real, *n*, and imaginary, *k*, parts of the complex refractive index for (a) the silicon substrate and (b) bulk $Ge_{23}Sb_7S_{70}$

This data plotted in Figure 4.8 was used to simulate the infrared transmission spectra of "ideal" films of various thicknesses. These ideal films have the same *n* and *k* as the bulk glass. The simulated spectra are shown in Figure 4.9 below. The thickness of the silicon substrate is 550 μm.

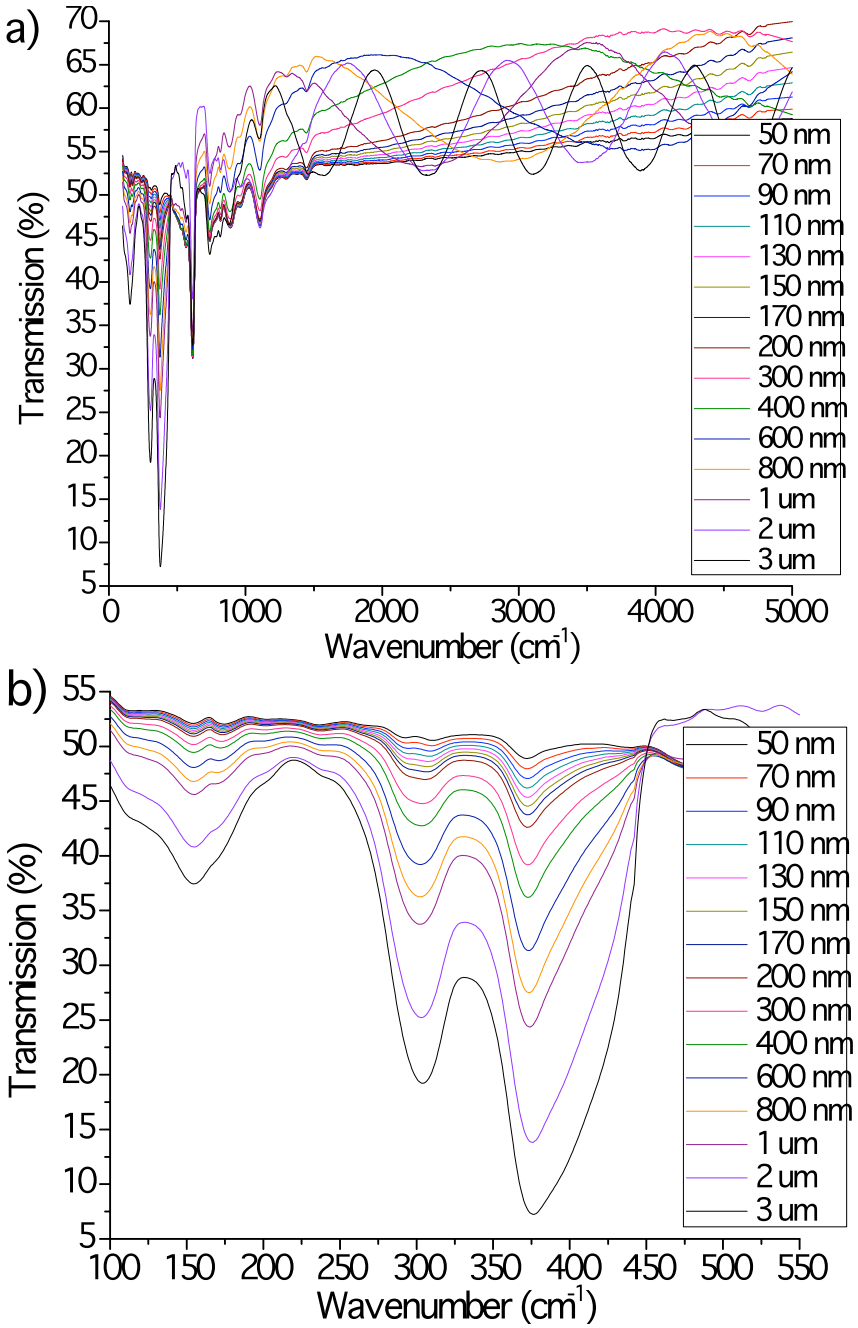

Figure 4.9: Simulation of $Ge_{23}Sb_7S_{70}$ films of various thicknesses with complex refractive index that matches that of the bulk. (a) Full FTIR spectra and (b) far-IR.

These simulated spectra can be used as a tool to make comparisons to deposited films. In Figure 4.9a, the fringes in the mid-IR region are caused by optical interference

from reflections at the multiple interfaces. The number of fringes increases as the film thickness increases. In Figure 4.9b, a detailed view of the far-IR region of the spectra is shown. While the optical interference in this region of the spectra is not as obvious as the fringes in the mid-IR, it can be seen that the shape of the absorption peaks changes with film thickness and there is also a slight shift of the peaks. For example, the peak at 372 cm^{-1} for films with thicknesses of 50-200 nm shifts to 377 cm^{-1} and a shoulder appears at ~425 cm^{-1} for all films with thicknesses above 800 nm. Also, the two peaks at 292 and 311 cm^{-1} for very thin films becomes one peak at 305 cm^{-1} for thicker films (>800 nm). These changes are caused by optical interference and are not due to changes of any properties of the glass, as the same input data was used for all the simulations in the figure. Then, the methodology is to fit the optical fringes in the mid-IR to estimate the film thickness. This allows accurate comparisons of peak shape, peak position, and the ratio of the size two or more peaks between simulated and experimental spectra to be made. This method allows analysis of differences between IR vibrational modes of the bulk glass as compared to the films.

Figure 4.10 shows the FTIR transmission spectrum of a 420 nm $Ge_{23}Sb_7S_{70}$ film deposited by thermal evaporation compared to a simulated spectrum of a 400 nm film. The TE film was not annealed following deposition.

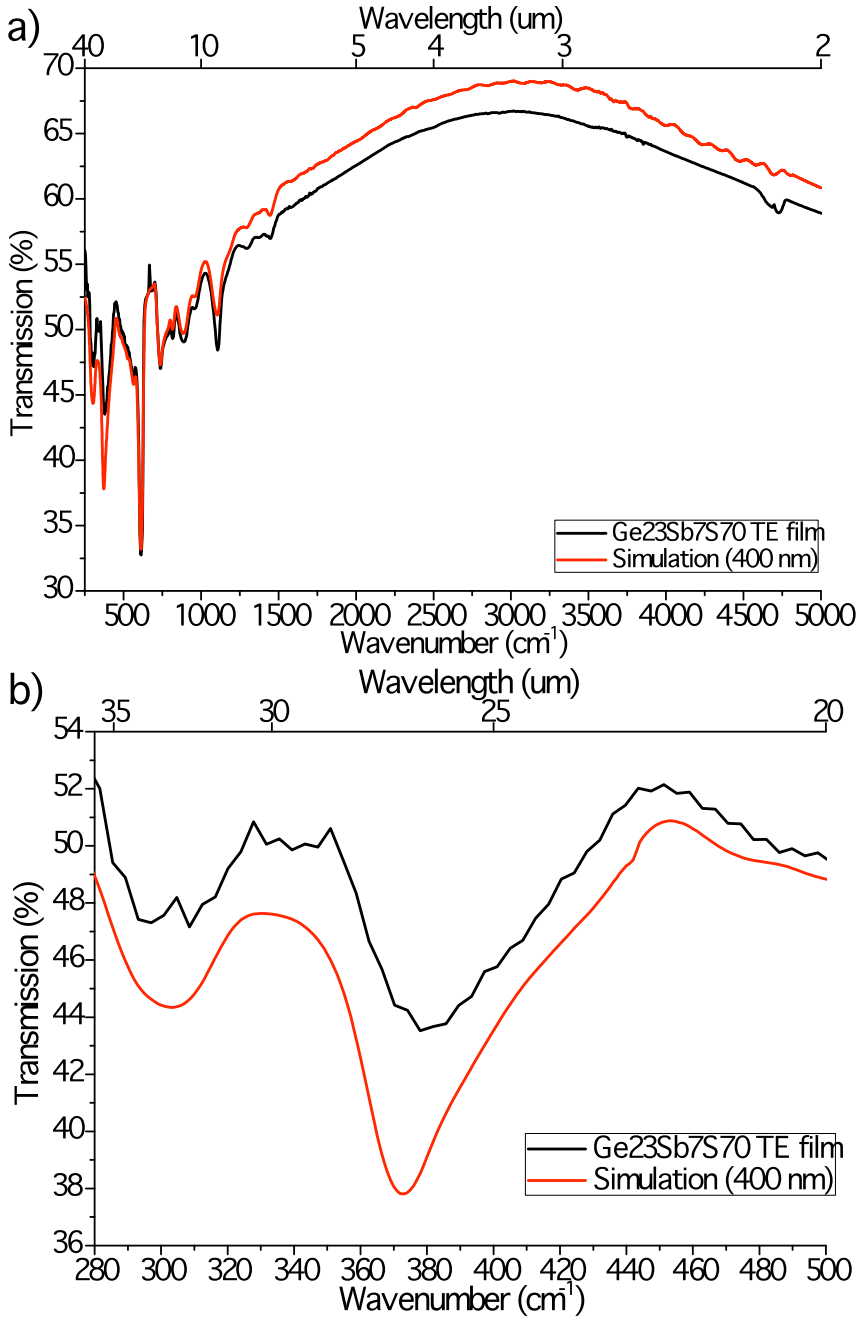

Figure 4.10: FTIR transmission spectrum of $Ge_{23}Sb_7S_{70}$ TE film compared to a simulated spectrum. (a) Full FTIR spectra and (b) far-IR.

The peaks at 615 and 1112 cm^{-1} are from the silicon substrate. In Figure 4.10a, the optical fringes in the mid-IR region match well, indicating that the TE film is

approximately 400 nm thick. In Figure 4.10b, the far-IR region is shown in detail. The main peak in the simulated spectrum is at approximately 370 cm^{-1} and the second peak is located at approximately 300 cm^{-1}. As was the case with the bulk glass, these peaks are related to the asymmetric stretching mode of GeS_4 tetrahedral units and the asymmetric stretching mode of SbS_3 trigonal pyramids, respectively [1,11]. For the experimentally measured spectrum of the TE film, the SbS_3 peak at 300 cm^{-1} appears to be two sharp peaks but this is due to changes in the atmosphere of the sample chamber during the measurement and not due to changes in the glass network. The main peak of the TE film is shifted from 370 cm^{-1} to 380 cm^{-1}. This shift has been attributed to the presence of non-bridging sulfur atoms in the glass network. This concept will be discussed in detail in Chapter 6.

4.4 Summary of Findings

The properties of the bulk glass and TE films discussed in this chapter are summarized below in Table 4.4 and 4.5, respectively.

Table 4.4: Summary of the optical properties of bulk $Ge_{23}Sb_7S_{70}$ and $Ge_{23}Sb_4S_{73}$

Property	**$Ge_{23}Sb_7S_{70}$**	**$Ge_{23}Sb_4S_{73}$**
Transmission Window	523 nm – 10.5 μm	513 nm – 10.5 μm
Refractive index at 880.7 nm	2.19	2.15
Structure	GeS_4 tetrahedra and SbS_3 trigonal pyramids; some S_8 rings	

Table 4.5: Summary of the properties of annealed TE $Ge_{23}Sb_7S_{70}$ films

Property	Value	Reference
Band Gap	2.48 eV (as-deposited) 2.54 eV (as-deposited) 2.61 eV (annealed)	Present study [3] [3]
Refractive index at 850 nm	2.21	[3]
Structure	GeS_4 tetrahedra and SbS_3 trigonal pyramids; less S_8 rings than bulk glass; some Ge-Ge bonds	[3]
Roughness	1.6 ± 0.3 nm	[13]
Transmission loss at 1550 nm	2.3 dB/cm	[4]

The bulk glass will be used as a reference material for the thin films discussed in the following chapters. The properties of the bulk glass will be compared to those of the solution-derived thin films with the goal being to produce thin films with the same properties as the bulk glass. The properties of thermally evaporated thin films, which have been routinely used in chemical sensors geometries in our group, will also be used as a point of reference, especially for physical properties such as roughness. The structure of TE films is clearly different than the bulk glass so for structural comparisons, the solution-derived films will be compared to the "ideal" IR spectra simulated using the optical constants of the bulk glass.

Based on all of this data, the "ideal" solution-derived film will have an index of ~2.19 at 880 nm, a band gap of ~2.6 eV, a structure made up of mostly GeS_4 tetrahedral units with SbS_3 trigonal pyramids. The roughness of the films should be less than 2 nm to avoid optical loss and the thickness should be ~800 nm for a source wavelength of 3-3.5 μm. The next chapter contains a discussion of the optimization of

the glass solutions in order to achieve a film with low surface roughness, little to no pinholes and/or cracking, and an appropriate thickness.

4.5 References

1. Petit L, Carlie N, Adamietz F, Couzi M, Rodriguez V, and Richardson KC. Correlation between physical, optical, and structural properties of sulfide glasses in the system Ge-Sb-S. *Materials Chemistry and Physics*. **97**, 64-70 (2006).
2. Gómez LA, Araújo CB, Putvinskis Jr R, Messaddeq SH, Ledemi Y, and Messaddeq Y. Nonlinear optical properties of antimony-germanium-sulfur glasses at 1560 nm. *Applied Physics B*. **94**, 499-502 (2009).
3. Musgraves JD, et al. Comparison of the optical, thermal and structural properties of Ge-Sb-S thin films deposited using thermal evaporation and pulsed laser deposition techniques. *Acta Materialia*. **59**, 5032-5039 (2011).
4. Hu J, Tarasov V, Agarwal A, Kimerling L, Carlie N, Petit L, and Richardson K. Fabrication and testing of planar chalcogenide waveguide integrated microfluidic sensor. *Optics Express*. **15**(5), 2307-2314 (2007).
5. Song S, Carlie N, Boudies J, Petit L, Richardson K, and Arnold CB. Spin-coating of $Ge_{23}Sb_7S_{70}$ chalcogenide glass thin films. *Journal of Non-Crystalline Solids*. **355**, 2272-2278 (2009).
6. Ma DS, Danielson PS, and Moynihan CT. Multiphonon absorption in XAs_2S_3-(1-X)GeS_2 glasses. *Journal of Non-Crystalline Solids*. **81**, 61-70 (1986).
7. Ma DS, Danielson PS, Moynihan CT. Bulk and impurity infrared absorption in 0.5 As_2Se_3-0.5$GeSe_2$ glass. *Journal of Non-Crystalline Solids*. **37**, 181-190 (1980).
8. Chu S, Li F, Tao H, Yang H, Wang S, Lin C, Zhao X, and Gong Q. SbS_3 enhanced ultrafast third-order optical nonlinearities of Ge-S chalcogenide glasses at 820 nm. *Optical Materials*. **31**, 193-195 (2008).
9. Petit L, Carlie N, Richardson K, Humeau A, Cherukulappurath S, and Boudebs G. Nonlinear optical properties of glasses in the system Ge/Ga-Sb-S/Se. *Optics Letters*. **31**(10), 1495-1497 (2006).
10. Kamitsos EI, Dussauze M, Varsamis CPE, Vinatier P, and Hamon Y. Thin film amorphous electrolytes: structure and composition by experimental and simulated infrared spectra. *Journal of Physical Chemistry C*. **111**, 8111-8119 (2007).
11. Charpentier F, Dussauze M, Cathelinaud M, Delaizir G, Kamitsos EI, Adam J-L, Bureau B, and Nazabal V. Aging process of photosensitive chalcogenide films deposited by electron beam deposition. *Journal of Alloys and Compounds*. **509**, 7330-7336 (2011).
12. Koudelka L, Frumar M, and Pisarcik M. Raman spectra of Ge-Sb-S system glasses in the S-rich region. *Journal of Non-Crystalline Solids*. **41**, 171-178 (1980).
13. Hu J. Planar chalcogenide glass materials and devices. PhD Thesis. Massachusetts Institute of Technology (2004).

14. Hu J, Feng N-N, Carlie N, Petit L, Agarwal A, Richardson K, and Kimerling L. Optical loss reduction in high-index-contrast chalcogenide glass waveguides via thermal reflow. *Optics Express*. **18**(2), 1469-1478 (2010).

CHAPTER FIVE

OPTIMIZATION OF GLASS SOLUTIONS

A solution-based spin-coating approach has previously been demonstrated for chalcogenide glass thin films [1-2] and was described in Chapter 3. The process is illustrated below in Figure 5.1. In this chapter, the focus is on optimizing the steps prior to the heat treatment.

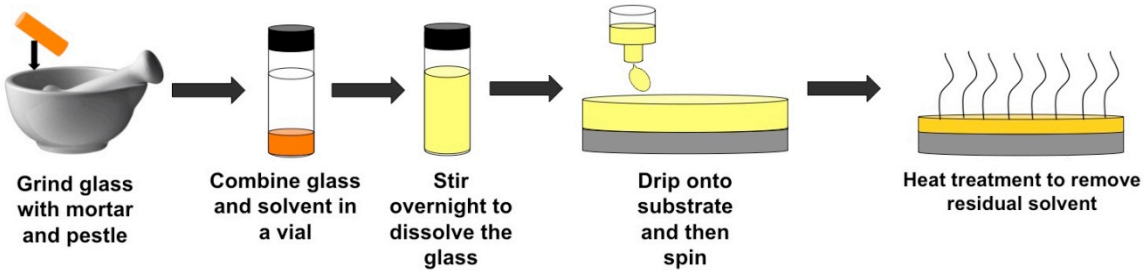

Figure 5.1: Illustration of the process for fabricating solution-derived films.

The figure shows all of the steps involved in the deposition of a film by spin coating. The glass is ground into a find powder and then dissolved in a solvent. The solvent is dried and a specific amount of water is added back into it before adding the glass. After the glass dissolves, it is dripped onto a substrate, spun at a specified speed for a specified time, and then heat-treated. In this chapter, the steps that will be discussed and optimized are the steps involving dissolution and deposition. The heat treatment step will be discussed in detail in Chapter 6.

Although exposure to water was mentioned in [1] with regards to causing precipitates, the effect of the water content of the solution has not been explored in detail. As water and hydroxyl ions have characteristic absorption bands near the target MIR

(source) wavelength of interest in our sensor application, the role of water, its presence in our glass films, its removal, and impact on film properties has been examined. This chapter will focus on how the water content of the solvent affects the dissolution of the glass powder and the roughness and surface quality of the deposited films. The effects of solution concentration and spin speed on the thickness, roughness, and surface quality of the films will also be discussed.

Film thickness is an important parameter to control in order to be able to properly couple light into the waveguides and resonator that will be fabricated from the films. Target film thickness is based on resonator design and the wavelength of the source light. Prior films used for 1.5μm studies had a target thickness of 400 nm. New applications using 3.2 μm light increase the target thickness to around 800 nm. For this reason, it is essential to know what film fabrication parameters are used to produce the desired film thickness. RMS roughness values should be less than 5 nm to ensure low optical loss in the films. High surface quality of a film will be defined as a film that has little to no cracking and/or pinholes on the surface.

For the solution-derived films in this study, propylamine was chosen as the solvent for several reasons. Amine solvents have previously been shown to be a more suitable choice for chalcogenide dissolution than hydroxides, which can form oxides with the glass [3]. Propylamine has a low boiling point of 48°C, so it evaporates quickly during the spin-coating process to form a glass film. The boiling point is well below the glass transition temperature of the glasses, allowing the films to be heat treated to drive off the solvent without risk of melting the glass.

5.1 Water Content in the Glass Solution

The effect of water content in the glass solution was studied for three glass compositions: As_2S_3, $Ge_{23}Sb_7S_{70}$, and $Ge_{23}Sb_4S_{73}$. Solutions were created by adding glass powder to 10 mL of anhydrous propylamine with a specific amount of de-ionized water added. Solutions were allowed to dissolve for several hours and were then visually inspected for precipitates. If no precipitates were seen with the naked eye, films were deposited from the solution. Films were soft baked for 3 minutes at ~50°C in a nitrogen atmosphere and then hard baked for 2 hours under vacuum at ~105°C. Film thickness and RMS roughness were measured using a Zygo (NewView 6300) white-light interferometric microscope.

The effect of water content on the RMS roughness of As_2S_3 films is presented below in Figure 5.2. The error bars are within the size of the data points for the films made with 26 μL of water added.

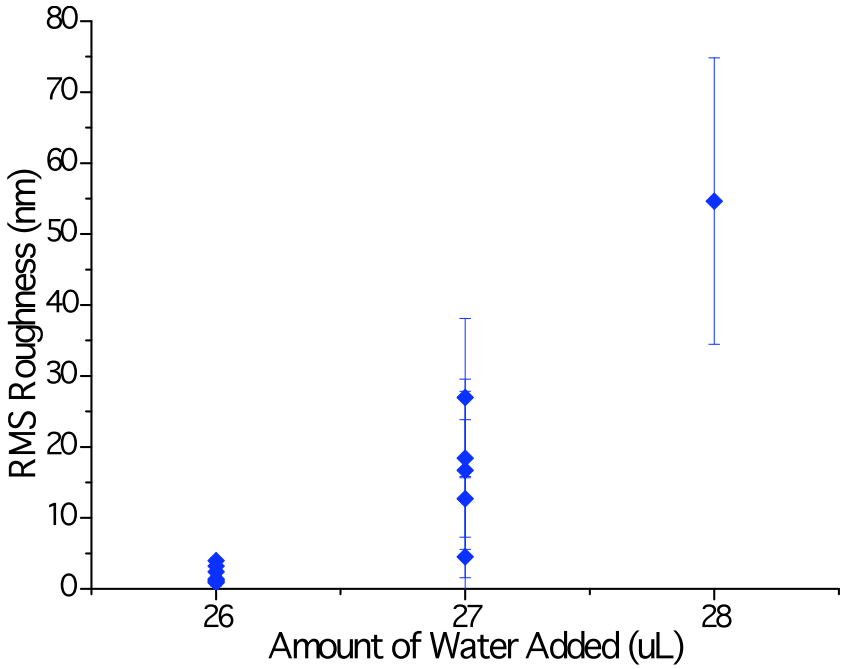

Figure 5.2: Effect of water content on RMS roughness of solution-derived As_2S_3 films deposited from a solution of 0.5 g of glass in 10 mL of PA (50 mg/mL).

The As_2S_3 solutions were found to form precipitates if the amount of water added to the 10 mL of propylamine was less than 26 µL or more than 28 µL. Within this small window of water content suitable for dissolution, a significant effect of water content on RMS roughness of the films is evident. The RMS roughness of these films increases dramatically from 1-2 nm for solutions with 26 µL of water to approximately 54 nm for those with 28 µL of water.

Besides affecting the RMS roughness, water content plays a role in the formation of cracks and pinholes on the film surface, which can lead to reduced optical quality. The surface profiles of two As_2S_3 films are shown in Figure 5.3 below. All parameters except the water content of the solution were the same for the two films. The film in Figure 5.3a was deposited from a solution with optimized water content (10 mL PA + 0.5 g As_2S_3 +

26 µL deionized water) while the film in Figure 5.3b was deposited from a solution containing excess water (10 mL PA + 0.5 g As_2S_3 + 29 µL deionized water). Films were deposited by spin coating at 4000 rpm for 10 s.

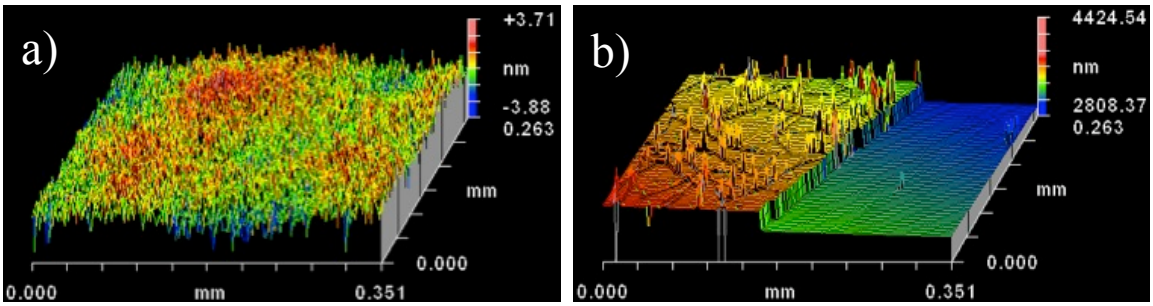

Figure 5.3: Surface profile of films made with a solution of 10 mL PA, 0.5 g As_2S_3, and (a) 26 µL or (b) 29 µL of deionized water. Spin coating was done at 4000 rpm for 10 s.

In Figure 5.3b, the orange area is the film whereas the blue/green area is the surface of the substrate where the film was removed to allow thickness measurements. The thickness of the film in Figure 5.3a was approximately 339 nm and the RMS roughness was approximately 1 nm. The thickness of the film in Figure 5.3b was approximately 310 nm but the cracking of the surface was too extensive to obtain an accurate RMS roughness measurement. It is clear that the optimization of water content in As_2S_3 glass solutions is crucial for fabricating films with low roughness and a crack free surface.

For As_2S_3 glass solutions, films must be deposited soon after dissolution because of the significant changes in film quality with small changes in water content. Another glass composition, $Ge_{23}Sb_7S_{70}$, was tested in an attempt to improve reproducibility. For this composition, previous efforts [3] have shown antimony to precipitate in glass loadings approaching 0.5 g of glass in 10 mL of PA (50 mg/mL) and to dissolve best

below around 0.25 g of glass in 10 mL of PA (25 mg/mL). For this reason, the initial solutions were made by dissolving 0.2 g of glass in 10 mL of anhydrous PA with various amounts of deionized water. The results are shown below in Figure 5.4.

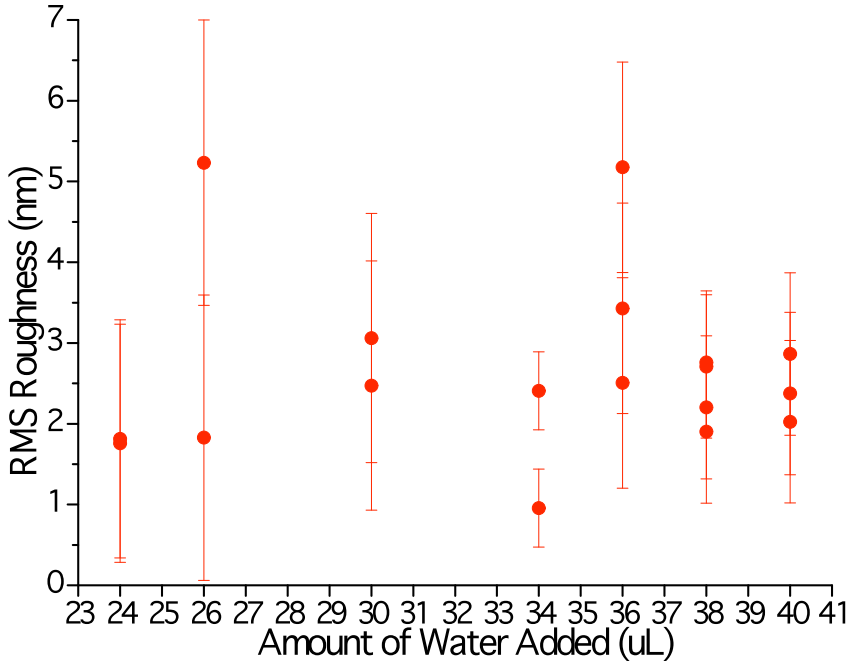

Figure 5.4: Effect of water content on RMS roughness of solution-derived $Ge_{23}Sb_7S_{70}$ films deposited from a solution of 0.2 g of glass in 10 mL of PA (20 mg/mL).

$Ge_{23}Sb_7S_{70}$ glass solutions were found to have a much larger range of water content needed for complete dissolution compared to As_2S_3 glass solutions. Also, it can be seen in the figure that the roughness is not significantly impacted by water content. Regardless of water content, the roughness of most of the films was in the 1-3 nm range, which is comparable to the target value of ~2 nm discussed in the previous chapter. Also discussed in the previous chapter was the fact that water impurities in GeSbS glasses cause absorptions in the 3-3.5 μm region of the source wavelength. In order to reduce water impurities, the solution that contains the least amount of water necessary for

complete dissolution while maintaining a low RMS roughness value is preferred. An appropriate water content of the solutions is necessary for complete dissolution, but it is important to remove it during the heat treatment to avoid loss due to absorption by H_2O and –OH impurities.

Because the glass solutions were found to be less sensitive to water content, making the results more reproducible, all subsequent experiments will focus on GeSbS compositions. The next section will discuss efforts to increase the thickness of these films in order to reach the target value of 800 nm.

5.2 Effects of Glass Loading and Spin Conditions on Film Thickness

For the purposes of this work, "glass loading" is defined as the mass concentration of the glass solutions in mg/mL. Films were deposited from solutions of $Ge_{23}Sb_7S_{70}$ and $Ge_{23}Sb_4S_{70}$ in PA with appropriate amounts of de-ionized water added to the solvent. The solutions were made with glass loading levels varying between 20 and 90 mg/mL. Figure 5.5 below shows the measured thickness variations of Ge23Sb7S70 and Ge23Sb4S73 films based on glass loading and spin speed.

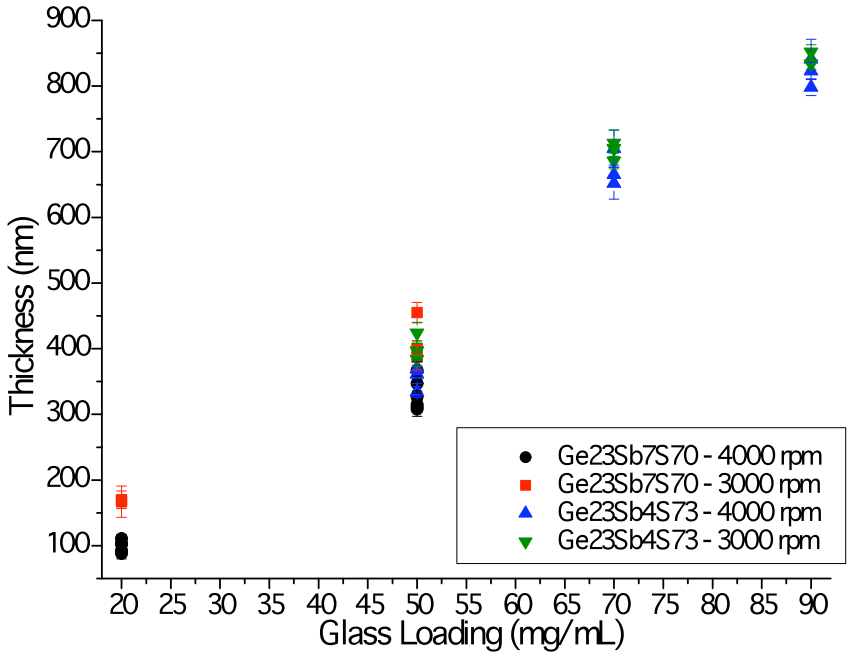

Figure 5.5: Effect of glass loading and spin speed on thickness of solution-derived chalcogenide glass thin films

As can be seen in the figure, thickness is directly related to the glass loading level of the parent solution. The increase in film thickness with increasing glass loading is due to an increase in the viscosity of the solution [3]. There is a small effect of the spin speed on the film thickness, with a lower spin speed yielding a slightly thicker film, but glass loading is the more important parameter of the two.

5.3 Summary of Findings

In this chapter, the glass solutions for spin-coating chalcogenide glass films were optimized and the effect of spin speed was studied. The results show that:

- The water content of the solvent influences dissolution of the glass and can thus affect the surface quality of the films.

- While spin speed plays a small role, glass loading is the key parameter for controlling the thickness of spin-coated films.

Based on the results discussed in this chapter, all of the solution-derived films in subsequent chapters have been made with the following recipe: 0.3 g of $Ge_{23}Sb_7S_{70}$ in 5 mL of propylamine with 18 µL of de-ionized water. All films were deposited by spin coating at 3000 rpm for 10 seconds. This chapter has studied the role of water content, glass loading, and spin conditions and optimized these parameters in order to produce films that meet the target roughness and thickness values. The heat treatment has been kept constant throughout these experiments, but now it must be studied in detail in order to meet the goal of producing films without any residual solvent. The next chapter will discuss the effects of various heat treatments on solvent removal, glass structure, glass-solvent interactions, and optical and physical properties of the films.

5.4 References

1. Chern GC and Lauks I. Spin-coated amorphous chalcogenide films. *Journal of Applied Physics*. **53**(10), 6979-6982 (1982).
2. Song S, Carlie N, Boudies J, Petit L, Richardson K, and Arnold CB. Spin-coating of $Ge_{23}Sb_7S_{70}$ chalcogenide glass thin films. *Journal of Non-Crystalline Solids*. **355**, 2272-2278 (2009).
3. Carlie N. A solution-based approach to the fabrication of novel chalcogenide glass materials and structures. PhD Thesis. Clemson University (2010).

CHAPTER SIX

CORRELATION BETWEEN STRUCTURE AND PROPERTIES OF SOLUTION-DERIVED CHALCOGENIDE GLASS THIN FILMS

The impact of the temperature and duration of the heat treatment used to cure solution-derived films on the final properties of the film will be studied in this chapter. The purpose of the heat treatment is to remove residual solvent and consolidate the glass network. The properties of the solvent and the glass are significantly different, so removing the solvent is important to obtain a film with properties matching those of the bulk glass. Ideally, the heat treatment would allow the fabrication of a film with no remaining solvent, low surface roughness, and little to no surface defects, such as cracks or pinholes, to avoid any optical loss.

6.1 Kinetics of Solvent Removal

Films in this chapter were deposited from a solution of 0.3 g $Ge_{23}Sb_7S_{70}$ in 5 mL of propylamine with 18 μL of water by spin coating at 3000 rpm for 10 seconds. In-situ IR measurements were used to track the removal of solvent from the films during heat treatments for various times and temperatures. First, the IR signature of the solvent must be known. Transmission FTIR spectra for propylamine and a solution of $Ge_{23}Sb_7S_{70}$ glass in propylamine are shown below in Figure 6.1.

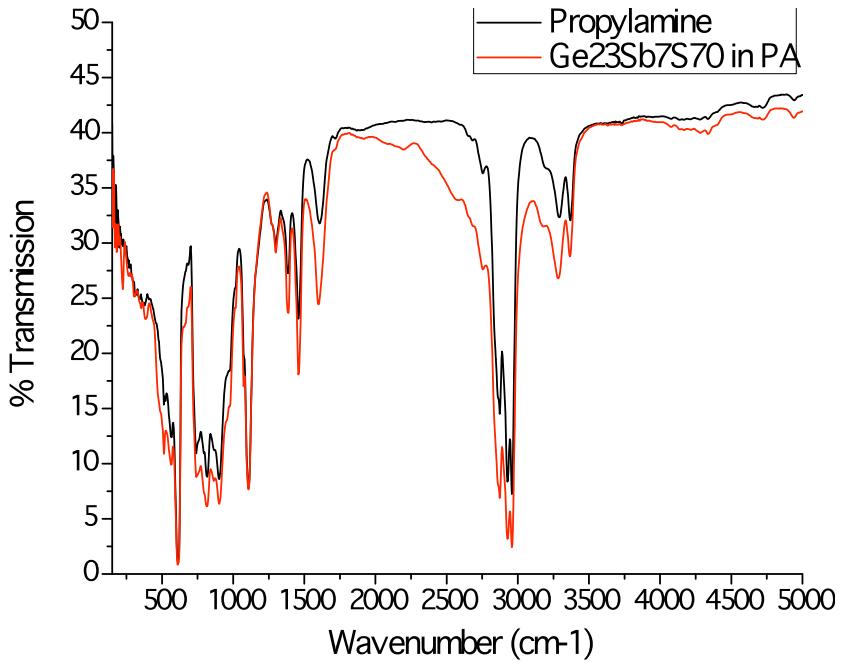

Figure 6.1: Transmission FTIR spectra of propylamine and $Ge_{23}Sb_7S_{70}$ in propylamine

A drop of the liquid was placed between two pieces of silicon in order to obtain the spectra in the figure. The main silicon absorption peaks are seen at 615 and 1112 cm^{-1} and are unrelated to the spectra of the propylamine or the glass solution. The main peaks from the solvent, which will be very important in measurements of the spin-coated films, are located in the region from 2500-3600 cm^{-1}. This region includes asymmetric and symmetric stretching modes of CH_3 at approximately 2960 and 2930 cm^{-1}, respectively [1]. There are also absorptions from the asymmetric stretching of NH_2 at 3398-3381 cm^{-1} and from the symmetric stretching of NH_2 at 3344-3324 cm^{-1}. No absorptions related to the glass network can be distinguished in the spectra. The main difference between the propylamine spectrum and the glass solution spectrum is that absorption bands from S-H appear in the region from 2600-2450 cm^{-1} [1]. This could be an indication of the

interactions between propylamine and dissolved ChG units. A summary of the absorption bands from propylamine can be found in Table 6.1 below.

Table 6.1: Summary of IR absorption bands of propylamine, taken from reference [1]

Absorption Band (cm^{-1})	**Assignment**
2975-2950	CH_3 – asymmetric stretching
2885-2865	CH_3 – symmetric stretching
1470-1440	CH_3 – asymmetric bending
2936-2915	CH_2 – asymmetric stretching
2865-2840	CH_2 – symmetric stretching
1475-1445	CH_2 – scissoring
1380-1370	-$C(CH_3)$ – symmetric bending
1385-1380, 1375-1365	-$C(CH_3)_2$ – symmetric bending
1395-1385, 1375-1365	-$C(CH_3)_3$ – symmetric bending
3398-3381	NH_2 – asymmetric stretching (dilute solution)
3344-3324	NH_2 – symmetric stretching (dilute solution)
1627-1590	NH_2 – scissoring
1090-1040	C-N – stretching
854-778	NH_2 – wagging (broad; liquid)
ca. 502 and 436	CCN – skeletal deformation
2600-2450	S-H – stretching

The amount of solvent remaining in a film was tracked by measuring the size of the CH_3 peak from propylamine (2960 cm^{-1}). This was done by drawing a tangent line across the absorption peak to act as a baseline and then measuring the distance (in % transmission) from the baseline to the tip of the peak. An example of this method is shown below in Figure 6.2. The red line is the baseline and the green line represents the measured size of the absorption peak. The absorption modes in the 2380-2290 cm^{-1} and 4000-3500 cm^{-1} regions are related to CO_2 and water, respectively, due to small changes in the atmosphere in the sample chamber between the background and the transmission spectra of the sample.

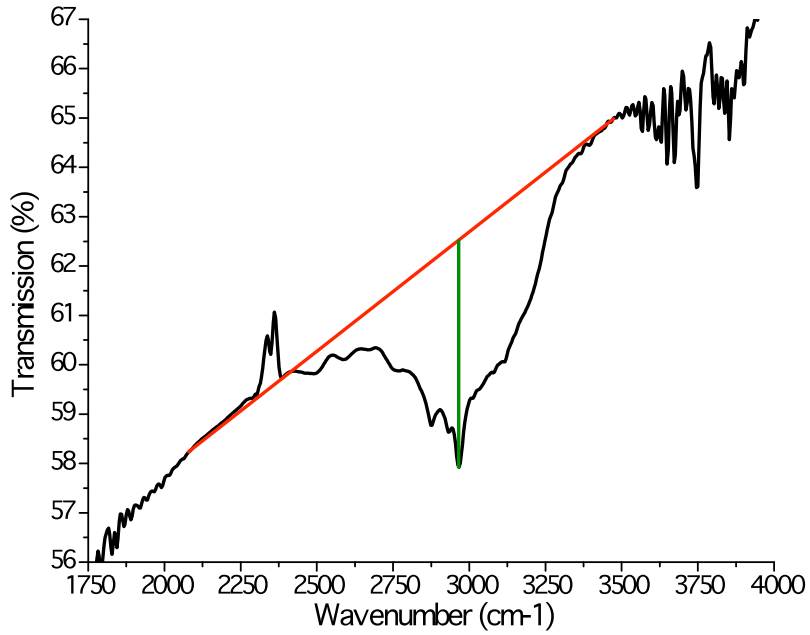

Figure 6.2: Schematic of the process of adding a baseline to determine the height of the CH_3 absorption peak from propylamine.

A film made from a solution of 5 mL of propylamine, 18 µL de-ionized water, and 0.3 g $Ge_{23}Sb_7S_{70}$ was deposited and soft-baked on a hot plate for 3 minutes at 50°C in a nitrogen atmosphere. An initial FTIR spectrum of this film was measured and then the film was hard baked with the following temperature profile: 3 hours at 98°C, 3 hours at 162°C, 2.5 hours at 180°C, and 1.5 hours at 198°C. During the heat treatment, an FTIR spectrum was measured every 5 minutes. The results were analyzed using the process described above and are shown below in Figure 6.3.

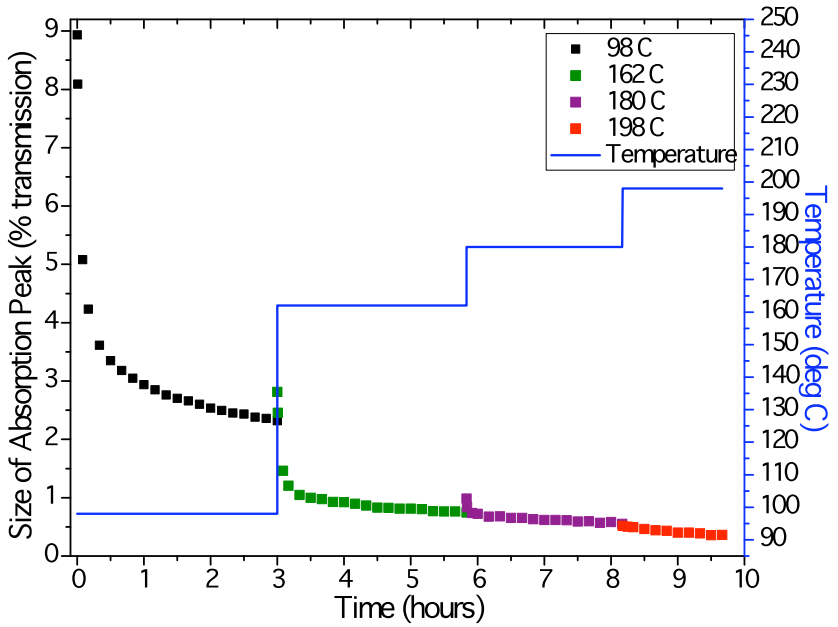

Figure 6.3: Kinetics of the reduction in the size of the solvent peak over the course of a multi-step heat treatment.

As seen in the figure, the solvent is removed rapidly following each temperature increase, especially at the 98°C and 162°C temperatures, but then the amount of solvent removed reaches a plateau fairly quickly at each temperature. Most of the solvent is loosely bonded in the film and approximately 67% can be removed fairly easily in the first half hour of baking at 98°C. A small percentage of the solvent is bonded strongly to the glass network—less than 1% of the residual solvent remains after the complete multi-step hard bake compared to the soft baked the film. Please note that the film was removed from the in-situ IR setup after the heat treatment at 98°C and the process was continued the following day after measuring a new background spectrum. Since the film was removed and then put back, it is possible that it was not in the exact same position. Due to some inhomogeneities in film thickness, this could account for the apparent increase in

solvent content after baking at 98°C. The same was done after the heat treatment at 162°C.

Based on the data in Figure 6.3, a shorter heat treatment was proposed. The new heat treatment was as follows: 1 hour at 98°C, 20 minutes at 162°C, 20 minutes at 180°C, and 20 minutes at 198°C. Again, a spectrum was recorded every 5 minutes and the data was analyzed as described previously. The results are shown below in Figure 6.4.

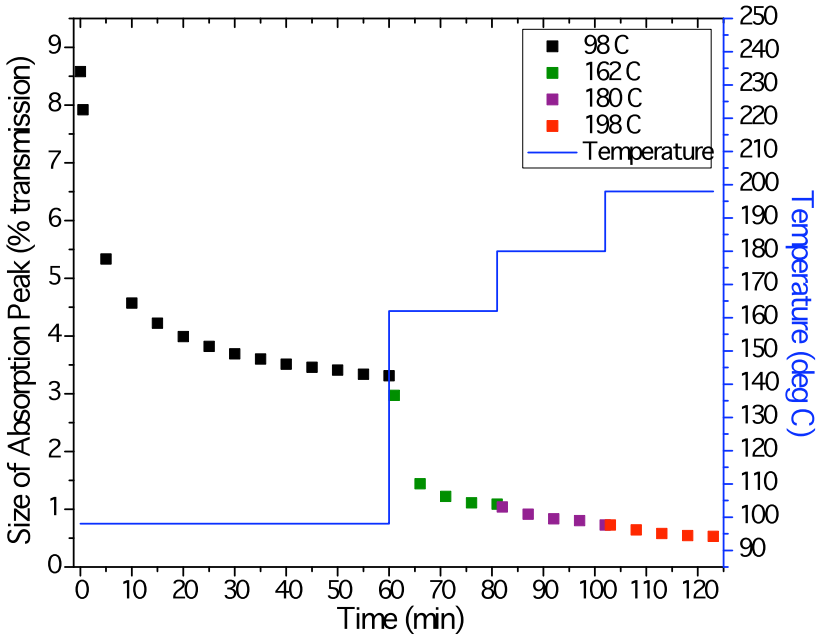

Figure 6.4: Kinetics of the reduction in the size of the solvent peak over the course of a revised multi-step heat treatment.

As seen in Figure 6.4, the final amount of solvent remaining is very similar to that of the film with the longer heat treatments, which confirms that the shorter heat treatment is sufficient.

It is important to know not only the kinetics of residual solvent removal, but also how the solvent interacts with the glass and how these interactions change over the course of the heat treatment. This will be discussed in the following section.

6.2 Glass Structure and Glass-Solvent Interactions

FTIR spectroscopy was used to investigate changes in the glass network structure and the glass-solvent interactions in the solution-derived films. However, the IR spectra of thin films must be considered carefully because the shape and position of absorption peaks can change due to optical interference as well as changes in the glass composition and structure. An optical model, which was discussed in detail in Chapter 4, was used to compare experimental spectra to a simulated spectrum of an "ideal" film with optical properties that match the parent bulk glass. Figure 6.5 shows the transmission spectra for a film after a few different heat treatments as well as a simulation of a 130 nm thick $Ge_{23}Sb_7S_{70}$.

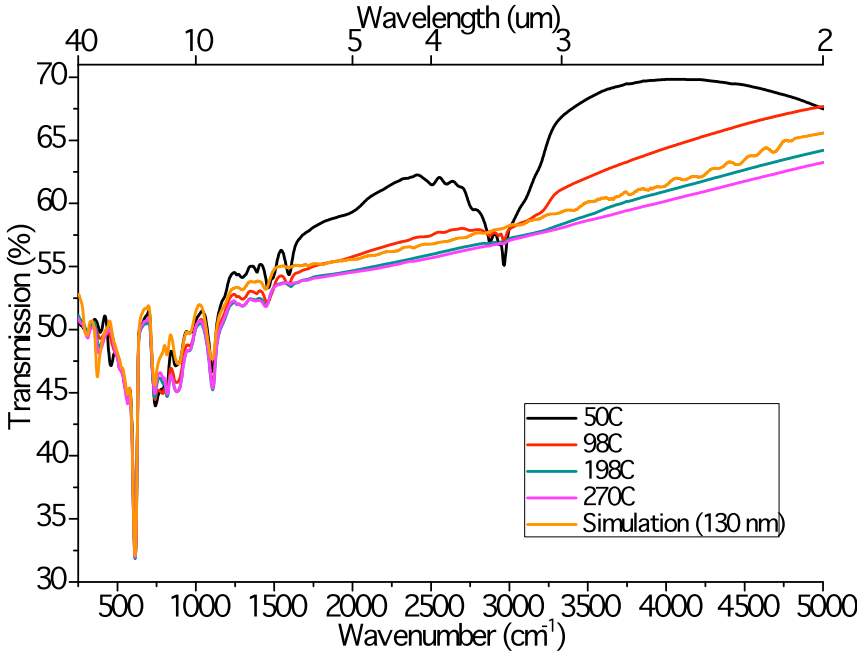

Figure 6.5: FTIR transmission spectra of $Ge_{23}Sb_7S_{70}$ films with various heat treatments.

The peaks at 615 and 1112 cm^{-1} are from the silicon substrate. The decreasing size of the fringes show the decrease in the thickness of the film and a dramatic decrease in the size of the solvent absorption peak can also be seen. In order to analyze how the structure of the glass network changes over the course of the heat treatment, it is necessary to analyze the far-IR spectra in detail. A detailed view of the far-IR region of the transmission spectra is shown below in Figure 6.6.

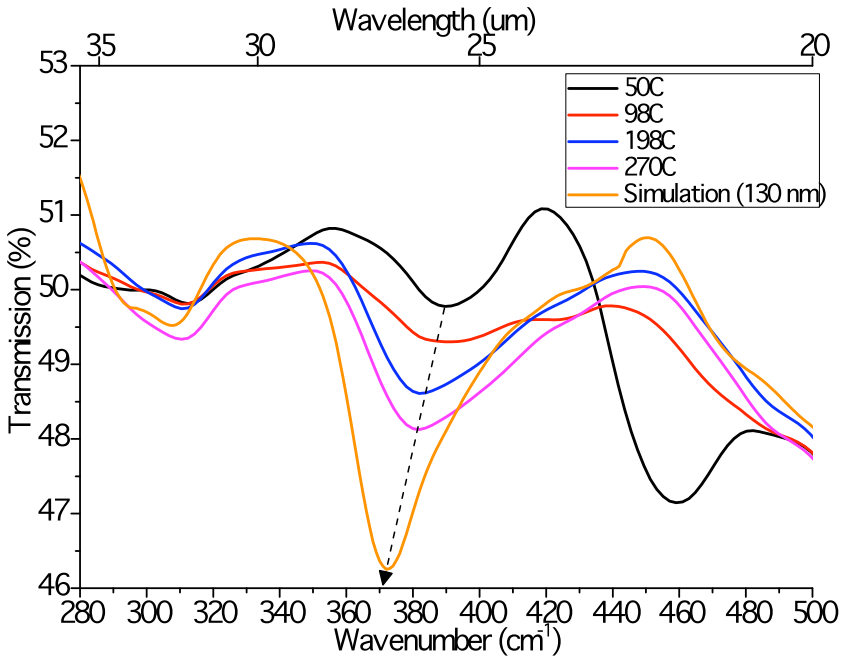

Figure 6.6: Far-IR transmission spectra of $Ge_{23}Sb_7S_{70}$ films with various heat treatments.

First, the absorption bands in the simulated spectrum will be discussed followed by an explanation of the thin film spectra and how it is believed that the glass network changes with heat treatment. The main absorption peaks for $Ge_{23}Sb_7S_{70}$ are the asymmetric stretching mode of $GeS_{Bridging}$ bonds in GeS_4 tetrahedral units at approximately 370 cm^{-1} and the asymmetric stretching mode of SbS_3 trigonal pyramids at 290-300 cm^{-1} [2-3]. The GeS_4 tetrahedra can be described as Q_n units, where n represents the number of bridging sulfur. The tetrahedral in the bulk glass used for the simulation are Q_4 units, so the peak at 370 cm^{-1} is attributed to Q_4 GeS_4 tetrahedra. For the film heat treated for 3 minutes at 50°C, a third peak appears at approximately 460 cm^{-1}. After heating at 98°C, the peak at 460 cm^{-1} disappears and the main peak starts to shift to lower wavenumber. This peak continues to shift to lower wavenumbers, towards that of the simulation at 370 cm^{-1}, after heating at higher temperatures.

A previous been study in reference [4] showed that as Na_2S was added to GeS_2, it acted as a network modifier and caused 2 moles of non-bridging sulfurs in the GeS_4 tetrahedra for every 1 mole of Na_2S added. For $40Na_2S$-$60GeS_2$, the main absorption band observed was at 450 cm^{-1} and was attributed to Q_2 GeS_4 tetrahedral units. For lower amounts of of Na_2S, such as the composition $20Na_2S$-$80GeS_2$, the main absorption band was at approximately 400 cm^{-1}, which is related to Q_3 units. As the amount of Na_2S continued to decrease, the peak at 400 cm^{-1} gradually shifted toward the absorption band of Q_4 units at 370 cm^{-1}.

There is a significant amount of residual solvent in the film baked at 50°C because it has not (at this point) undergone a hard bake heat treatment. It is thought that in this case the solvent, as part of the bulk glass dissolution process, has broken up the network and causes the presence of two non-bridging sulfur atoms in the GeS_4 tetrahedra, as was described for the Na_2S-modified glass. Therefore, after a soft bake at 50°C the glass network is made up of mostly Q_2 units. Since the Q_2 GeS_4 tetrahedral units have two non-bridging sulfur atoms, the structure of the glass is likely mostly made up of Ge-S chains with propylamine molecules bonded along the chain. After heating the film at 98°C, the absorption band related to Q_2 units disappears, suggesting that as the solvent begins to be removed, the film's network begins to become more polymerized, forming bridging sulfurs within and between tetrahedral. While the main network peak associated with the GeS_4 units is located at approximately 385 cm^{-1}, its offset from 370 cm^{-1} that is seen in a fully polymerized bulk material suggests that there are still some non-bridging sulfur atoms remaining, most likely in the form of a lone non-bridging sulfur atom on an

otherwise bridging Ge-S containing tetrahedra. At this point, the glass network is composed of both Q_3 and Q_4 units because the main peak is still shifted from the 370 cm^{-1} band that is seen in the fully polymerized glass. As the film is heated at higher temperatures, the peak shifts to lower wavenumbers as indicated by the arrow. This suggests that the network ratio of Q_4/Q_3 units is increasing because the peak is approaching the position main peak in the simulated spectrum. The peak also grows in size even though the films are decreasing in thickness. This confirms that the glass network is moving towards a fully polymerized, condensed state and becomes more connected as the solvent is removed. However, as can be seen the heat treatment times and temperatures used to this point, do not fully reach the structural arrangement suggested by the simulation of a fully condensed, 130 nm glass film. Therefore, the final structure of the film is still a combination of Q_4 and Q_3 GeS_4 tetrahedral units. One might expect that further treatment could allow this state to be realized. However, this could perhaps be at the expense of film optical quality. A summary of the IR absorption bands for the far-IR region is presented in Table 6.2 below.

Table 6.2: Summary of far-IR absorption bands of $Ge_{23}Sb_7S_{70}$ thin films

Absorption Band (cm^{-1})	**Assignment**	**Reference**
290-300	SbS_3 trigonal pyramids – asymmetric stretching mode	[2-3]
335	SbS_3 trigonal pyramids – symmetric stretching mode	[2]
370	Q_4 GeS_4 tetrahedral units- asymmetric stretching mode	[4]
390-400	Q_3 GeS_4 tetrahedral units- asymmetric stretching mode	[4]
450	Ge-$S_{non\text{-}bridging}$ bonds in Q_2 GeS_4 tetrahedra	[4]

To further investigate the role of solvent removal in the formation of the glass network, a detailed view of the mid-IR region from 2400-3500 cm^{-1} is presented below in Figure 6.7. For this figure, the transmission data from Figure 6.5 has been converted to absorbance and normalized to the CH_3 absorption peak at 2960 cm^{-1}.

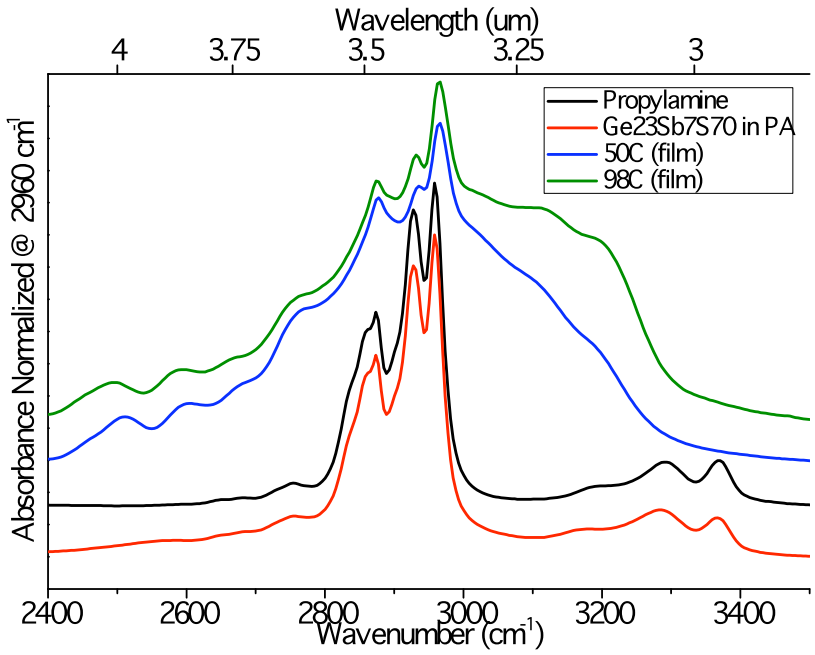

Figure 6.7: Mid-IR absorbance of $Ge_{23}Sb_7S_{70}$ films with various heat treatments normalized to absorbance of CH_3 at 2960 cm^{-1}.

The main peaks in the figure have already been discussed with regards to the IR spectra for propylamine as well as the solution of $Ge_{23}Sb_7S_{70}$ in propylamine. The peaks at 2960 and 2930 cm^{-1} are related to the asymmetric stretching modes of CH_3 and CH_2, respectively [1]. The third main peak is a combination of the symmetric stretching modes of CH_3 and CH_2 at 2870 and 2850 cm^{-1}, respectively [1]. Peaks from the asymmetric stretching of NH_2 at 3398-3381 cm^{-1} and from the symmetric stretching of NH_2 at 3344-3324 cm^{-1} can be seen in the spectra for propylamine and the glass solution [1]. However,

these bonds are not seen in the spectra of the films baked at different temperatures. Instead, absorptions from stretching of R-NH_3^+ salts appear at approximately 3200-2800 cm^{-1} and there is an increase in the relative intensity of these bands with baking temperature [1]. Another absorption that is seen for the films is from the stretching of S-H bonds in the region from 2600-2450 cm^{-1} [1]. Based on this information, the structure shown in Figure 6.8 has been proposed to represent glass-solvent interactions in the spin-coated films.

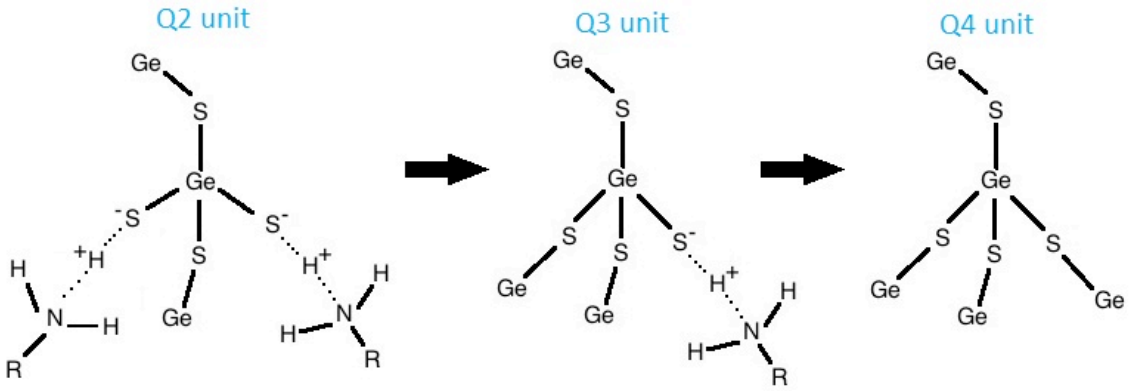

Figure 6.8: Proposed structures of glass-solvent interactions in spin-coated $Ge_{23}Sb_7S_{70}$ thin films.

The figure shows the progression of the glass-solvent interactions during the heat treatment process. A film that has only been soft baked at 50°C will contain mostly Q_2 units with a small amount of Q_3 units. This film is made up of GeS chains with two propylamine molecules bonded to each Ge atom along the chains. During the hard bake at 98°C, enough propylamine is removed so that the film is comprised of a combination of Q_3 and Q_4 units. More propylamine is removed as the film is baked at higher and higher temperatures and the ratio of Q_4/Q_3 units steadily increases. However, a film

entirely made up of Q_4 units was not achieved in this study even after annealing at 270°C. The hydrogen atom linking the glass network to the solvent is believed to be from the water that is added to the glass solution during dissolution. The bonds between the non-bridging sulfur in the GeS_4 tetrahedra and the propylamine are very strong and this explains why it is hard to remove all of the solvent even at temperatures much higher than the boiling point of the solvent, which is 48°C.

Changes in the optical and physical properties of solution-derived films with heat treatment will now be studied and correlated with the structural changes discussed above.

6.3 Optical Properties

Propylamine has very different optical properties than bulk $Ge_{23}Sb_7S_{70}$ glass, so it is important to study the effects of solvent removal on the band gap and refractive index of the films. In-situ UV-Vis measurements were made with the similar process to the one used for in-situ IR measurements. An absorption spectrum was recorded every 5 minutes as the film was being heated. In order to study the kinetics, the absorption at 310 nm was plotted as a function of time and temperature. The results are presented below in Figure 6.9.

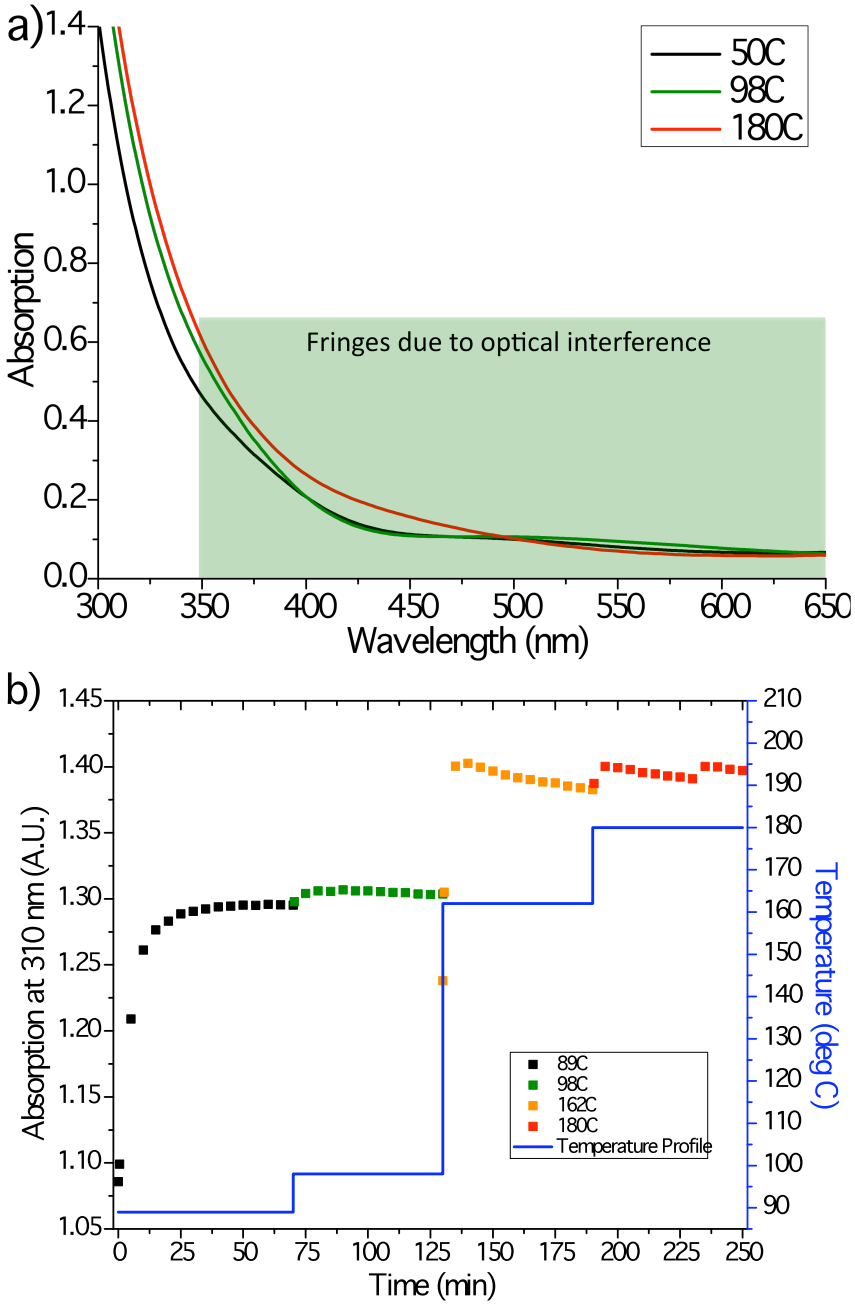

Figure 6.9: (a) UV-vis absorption spectra and (b) kinetics of the change in absorption at 310 nm for a solution-derived $Ge_{23}Sb_7S_{70}$ thin film over the course of a multi-step heat treatment.

As seen can be seen in Figure 6.9a, the cutoff wavelength of the $Ge_{23}Sb_7S_{70}$ solution-derived films shifts toward higher wavelengths with increasing heat treatment

temperature for the films. Figure 6.9b shows that the absorption at 310 nm increases quickly following each temperature change and then reaches a plateau, similar to the kinetics of the solvent peak reduction. There is an anomaly at the higher heat treatment temperatures because the absorption appears to decrease after the initial increase. This could be related to changes in optical interference fringes as the film decreases in thickness over the course of the heat treatment.

To compare with the TE reference films, the band gap must be estimated by constructing a Tauc plot. The method for making a Tauc plot for thin films was described in Chapter 3. The Tauc plots are shown in Figure 6.10 below. An important note is that the film thicknesses used in the calculations were estimated. The thicknesses of films with these heat treatments, but deposited on silicon substrates, were measured using ellipsometry. However, the film used for the in-situ UV-vis measurements was deposited on a glass slide and the thicknesses could be slightly different, which would change the calculated value of the band gap.

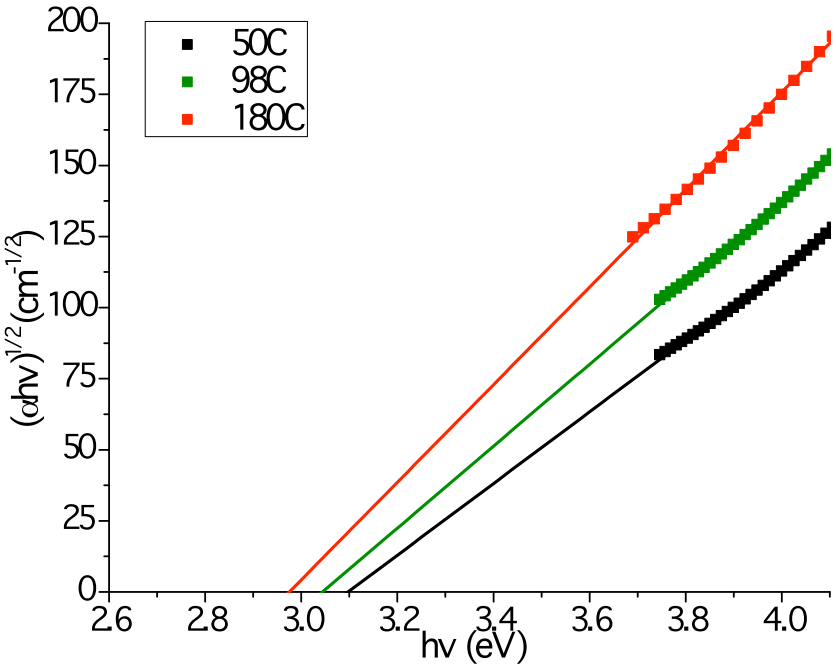

Figure 6.10: Calculated Tauc plots of $Ge_{23}Sb_7S_{70}$ thin films with various heat treatments

The optical band gap of the films was found by performing a linear curve fit on the linear section of the curves, between approximately 3.7 and 4.2 eV. Then, the linear curve fit was extrapolated to find the x-intercept. As seen in the figure, the band gap shifts to lower energy at higher heat treatment temperatures. The band gap decreases from 3.10 eV at 50°C to 3.04 eV at 98°C and then 2.97 eV at 180°C. The band gap of these solution-derived films is higher than the band gap of films deposited by thermal evaporation and pulsed laser deposition, which are 2.61 and 2.72 eV, respectively, after annealing [5].

Another important optical property that is affected by solvent removal is the refractive index. Dispersion curves for the refractive index of bulk $Ge_{23}Sb_7S_{70}$ and solution-derived films with various heat treatments are shown in Figure 6.11.

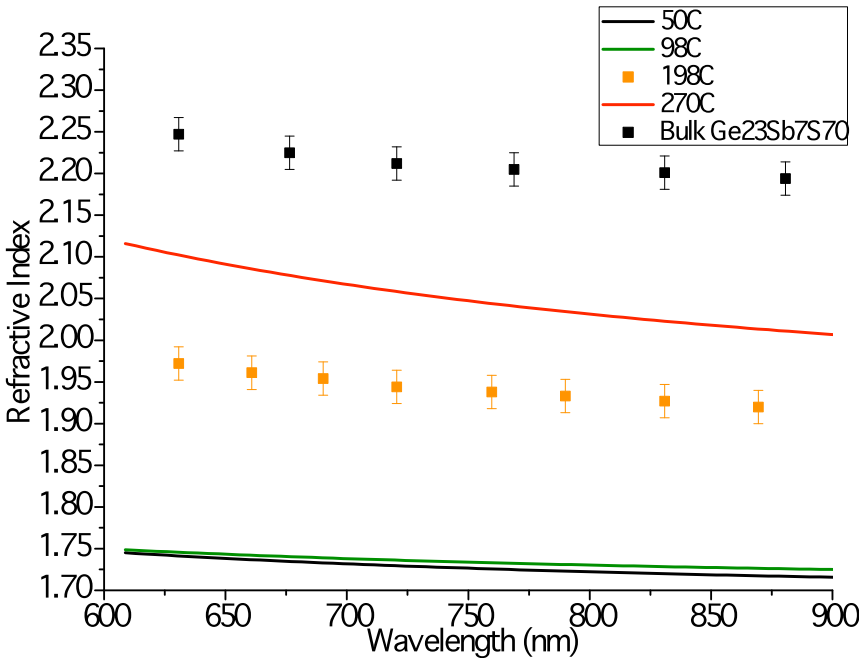

Figure 6.11: Comparison of the refractive index dispersion curves of films with various heat treatments and the parent bulk glass

For the films that have a solid line for the dispersion curve, a Cauchy model was applied to data from several measurements in the region shown. For the bulk glass and the film baked at 198°C, an acceptable fit could not be made with the model, so an index was calculated for each wavelength measured. The index increases significantly with increasing heat treatment temperature. This can be attributed to the removal of the propylamine solvent, which has a much lower refractive index (n = 1.388) compared to the glass. Even after annealing the film at 270°C, which is 40°C below T_g, the refractive index is lower than the bulk glass. The refractive index of TE and PLD films has been reported to be 2.21 (at 842 nm) and 2.27 (at 898 nm), respectively [5]. These indices are very close that of the bulk glass and higher than that of the solution derived films.

There is a small amount of residual solvent remaining in the film even after annealing at 270°C, which could partially explain the differences in band gap and refractive index between the solution-derived and TE films. However, another possibility is the creation of pores in the film as the solvent is removed. The formation of pores during solvent removal has also been seen in other studies on solution-derived chalcogenide films [6]. To further illustrate this point, the refractive index is plotted as a function of the size of the propylamine absorption peak at 2960 cm^{-1} in Figure 6.12. The size of the propylamine absorption peak is directly proportional to the amount of solvent in the thin film.

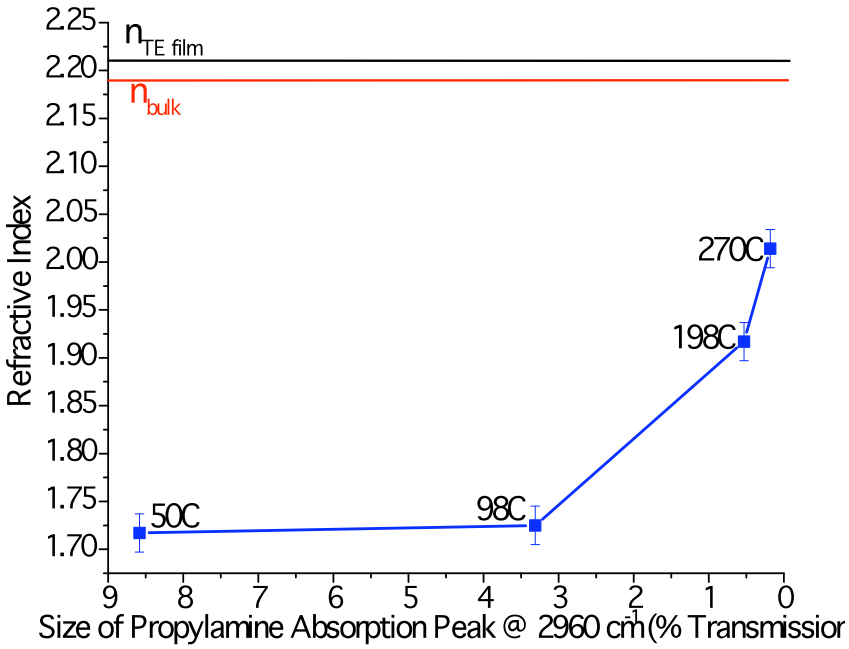

Figure 6.12: Refractive index as a function of residual solvent

As seen in the figure, the index does not increase significantly until the amount of residual solvent is very low. Even after removing about 2/3 of the residual solvent, the index only increases from n = 1.717 to n = 1.725. The index then increases rapidly with

heat treatments at higher temperatures, even though further changes in the size of the propylamine absorption peak are small. It is hypothesized that even though most of the solvent is removed by heat treating at 98°C, there are pores left behind as the solvent escapes the glass network and it takes higher temperatures to further densify the film and increase the index. AFM measurements were made in an attempt to confirm this assumption.

6.4 Physical Properties

Surface quality is an important parameter to consider when analyzing thin films. A high surface roughness or features such as pinholes and cracking will result in optical loss in the film. AFM was used to measure roughness and to inspect the topography of the surface of the films. AFM images for films heat treated at various temperatures are shown in Figure 6.13.

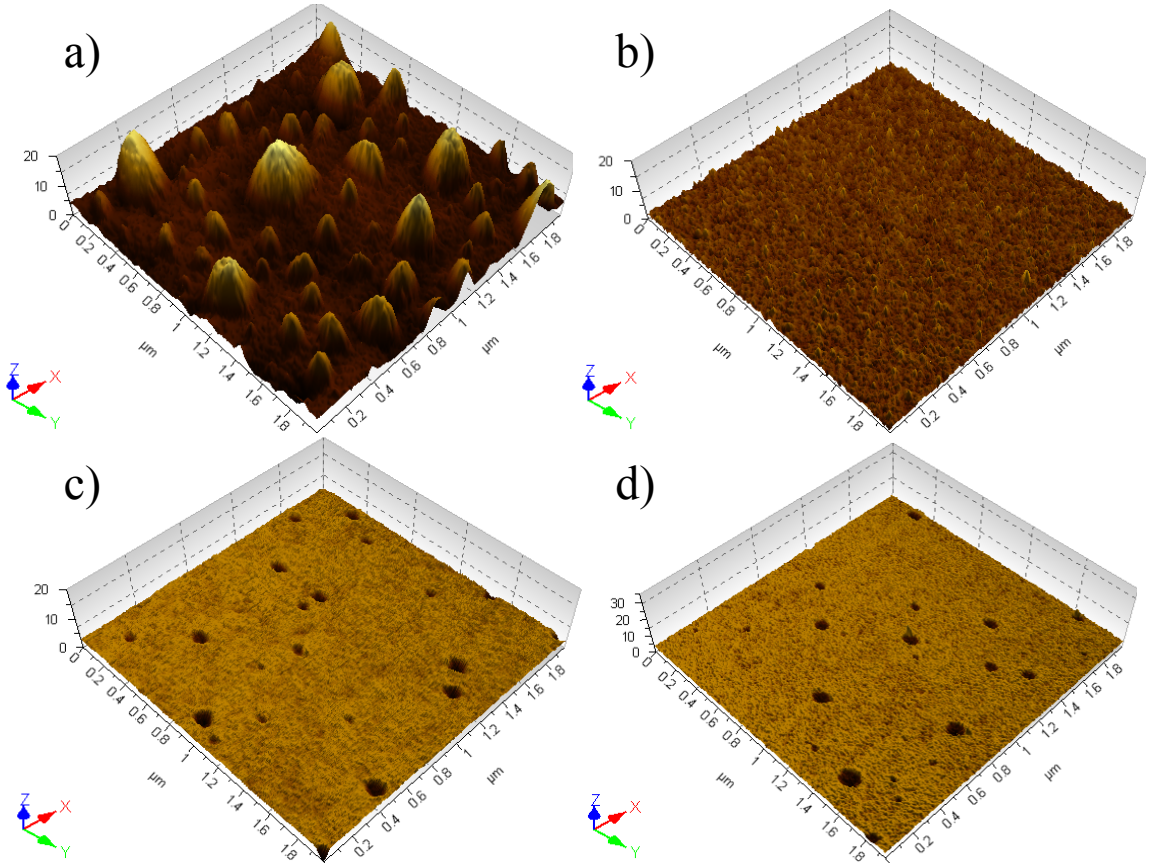

Figure 6.13: AFM images of the topography of the surface of a solution-derived $Ge_{23}Sb_7S_{70}$ thin film after heat treatment at (a) 50°C (b) 98°C (c) 198°C and (d) 270°C.

The topography of the films changes dramatically over the course of the heat treatment. After a soft bake for 3 minutes at 50°C, there are many "bumps" or "bubbles" across the surface of the film. Then the surface becomes relatively flat after being heated at 98°C for 1 hour. Holes form on the surface of the film after heat-treating up to 198°C and these holes remain after annealing the film for 1 hour at 270°C. The height and diameter of the bubbles seen in Figure 6.13a were measured, as shown below in Figure 6.14.

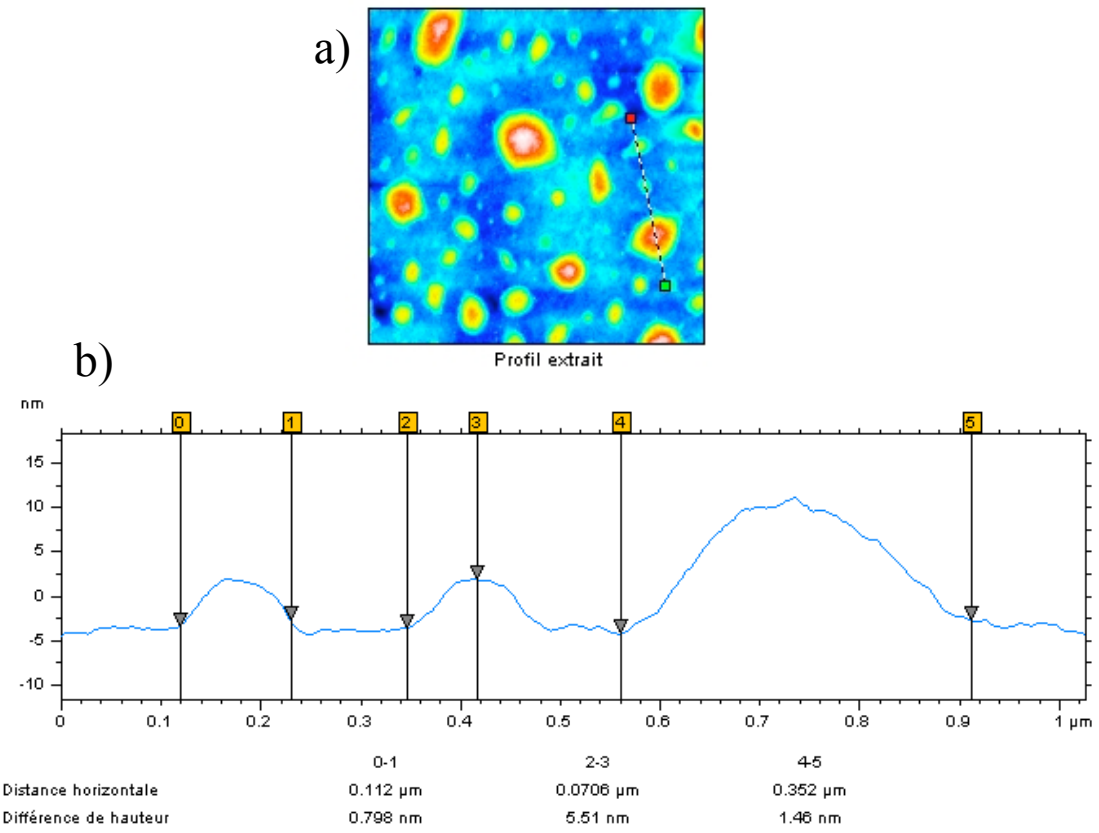

Figure 6.14: (a) 2x2 µm square topographical map of the surface of a $Ge_{23}Sb_7S_{70}$ film baked at 50°C. The profile of the line drawn has been extracted and is shown in (b).

As seen in the figure, the width of the bubbles ranges from approximately 100 nm to over 350 nm and the height is between 6-20 nm. These bubbles may be due to solvent trapped in the film. Figure 6.15 below shows the profile of a larger area on the same film.

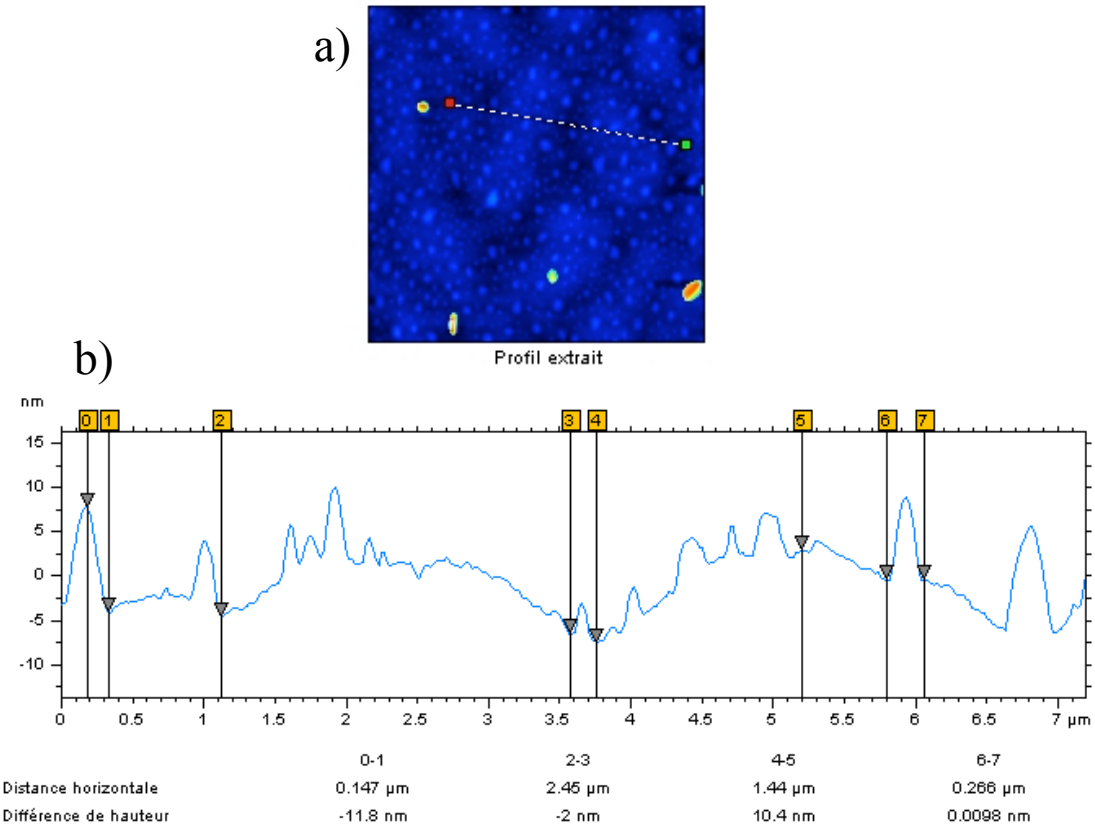

Figure 6.15: (a) 8x8 µm square topographical map of the surface of a $Ge_{23}Sb_7S_{70}$ film baked at 50°C. The profile of the line drawn has been extracted and is shown in (b).

Figure 6.15 shows that, along with the small bubbles across the surface, there is some inhomogeneity of the film thickness. The width of these areas is approximately 2.45 µm ("distance horizontale" between markers 2 and 3) and the height is approximately 10.4 nm ("difference de hauteur" between markers 4 and 5).

After a hard bake for 1 hour at 98°C, the bubbles disappear and the thickness becomes more homogeneous across the surface as seen in Figure 6.16.

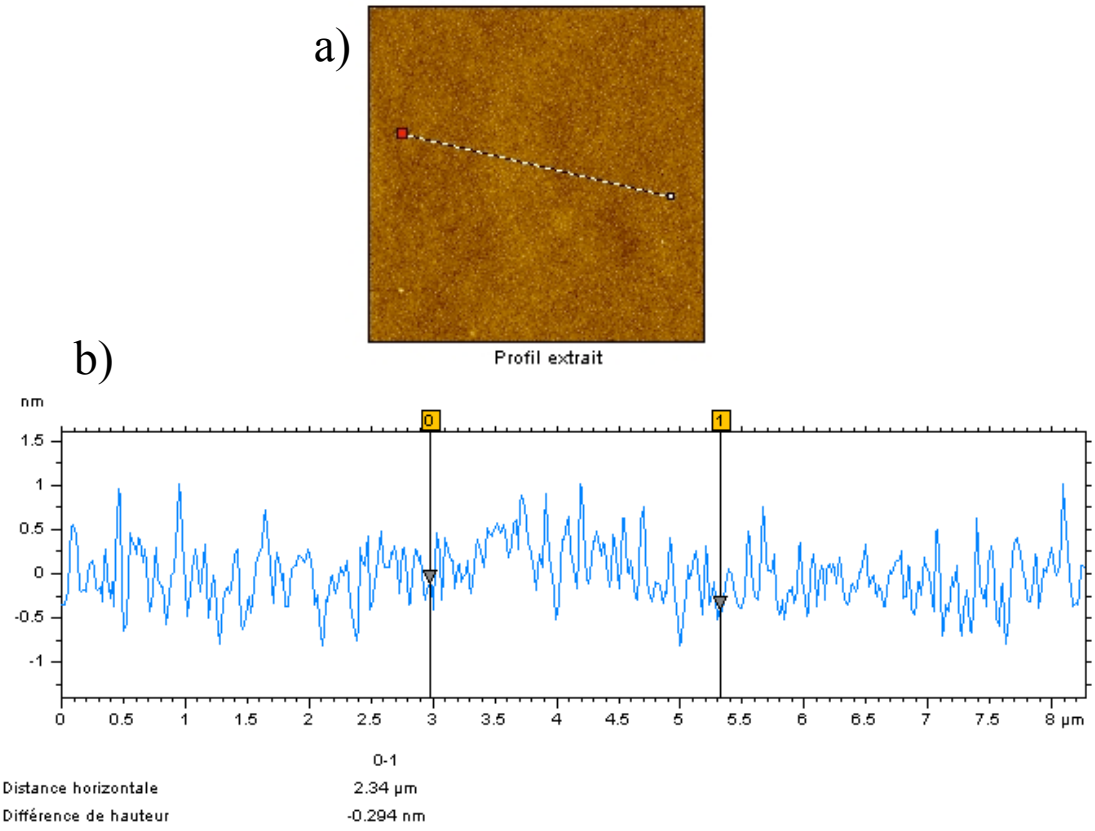

Figure 6.16: (a) 10x10 µm square topographical map of the surface of a $Ge_{23}Sb_7S_{70}$ film baked at 98°C. The profile of the line drawn has been extracted and is shown in (b).

There are no significant thickness changes across the surface of this film and there is no sign of the bubbles that were seen on the film that was only soft baked at 50°C. There are also no pinholes seen on the surface of the film. After heating at higher temperatures, as seen in the surface profile in Figure 6.17 below, pinholes appear on the surface of the film.

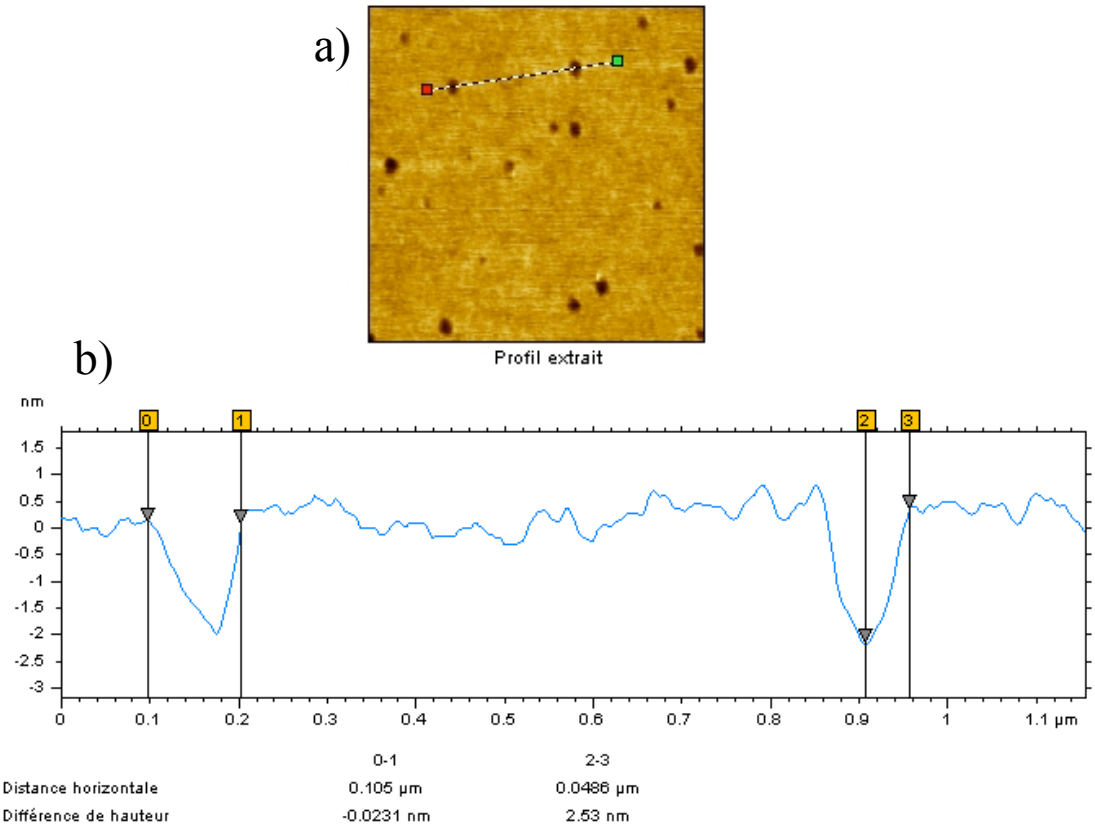

Figure 6.17: (a) 2x2 µm square topographical map of the surface of a $Ge_{23}Sb_7S_{70}$ film baked at 198°C. The profile of the line drawn has been extracted and is shown in (b).

As determined from Figure 6.17b, the width of the holes is in the 100 nm region and the height is approximately 2.5 nm. This width is similar to that of the bubbles seen in Figure 6.14. The holes are smaller than the 200 nm diameter pores seen in previous studies [6].

After annealing the film at 270°C in an attempt to improve the surface quality, the holes still remain. A surface profile of a film annealed at 270°C for 1 hour following the multi-step heat treatment described previously is shown in Figure 6.18.

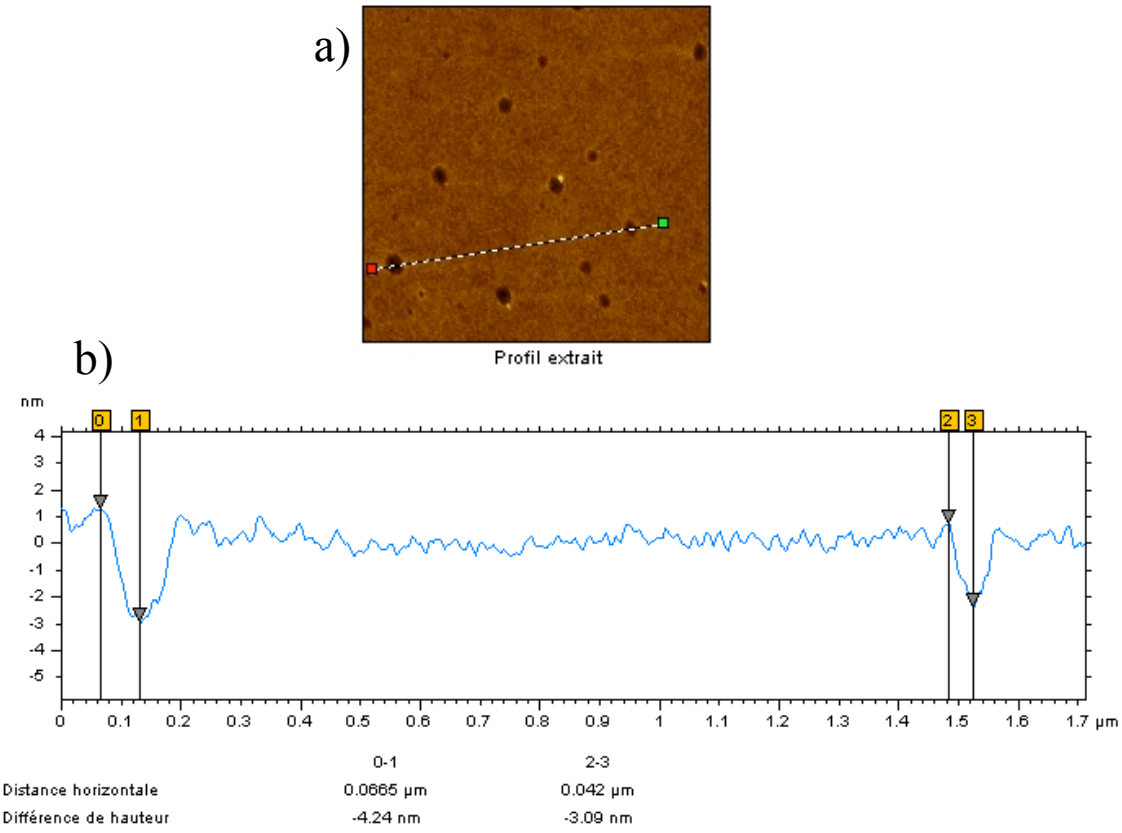

Figure 6.18: (a) 2x2 µm square topographical map of the surface of a $Ge_{23}Sb_7S_{70}$ film annealed at 270°C. The profile of the line drawn has been extracted and is shown in (b).

The holes in the annealed film are a few nanometers deep and in the range of 100 nm wide. This is similar to the dimensions of the holes before this step of the heat treatment, so annealing the film at 270°C does not appear to have a significant effect on the surface quality.

Although it does not affect the surface quality significantly, a positive aspect of annealing the film is that it increases the index, as was shown previously in Figures 6.11 and 6.12. This is believed to be due to a further densification of the glass network rather than the elimination of pinholes from the film surface. The pinholes seen in the films baked at high temperatures are believed to be due to the presence of pores left behind as

the propylamine, which makes up a large percentage of the original film, is removed from the glass network. This could explain why the index remains low after removing a large percentage of the residual solvent.

To further explore the changes in the film properties with increasing heat treatment temperatures, the changes in thickness, roughness, refractive index, and amount of residual solvent with increasing heat treatment temperature are plotted in Figure 6.19 below.

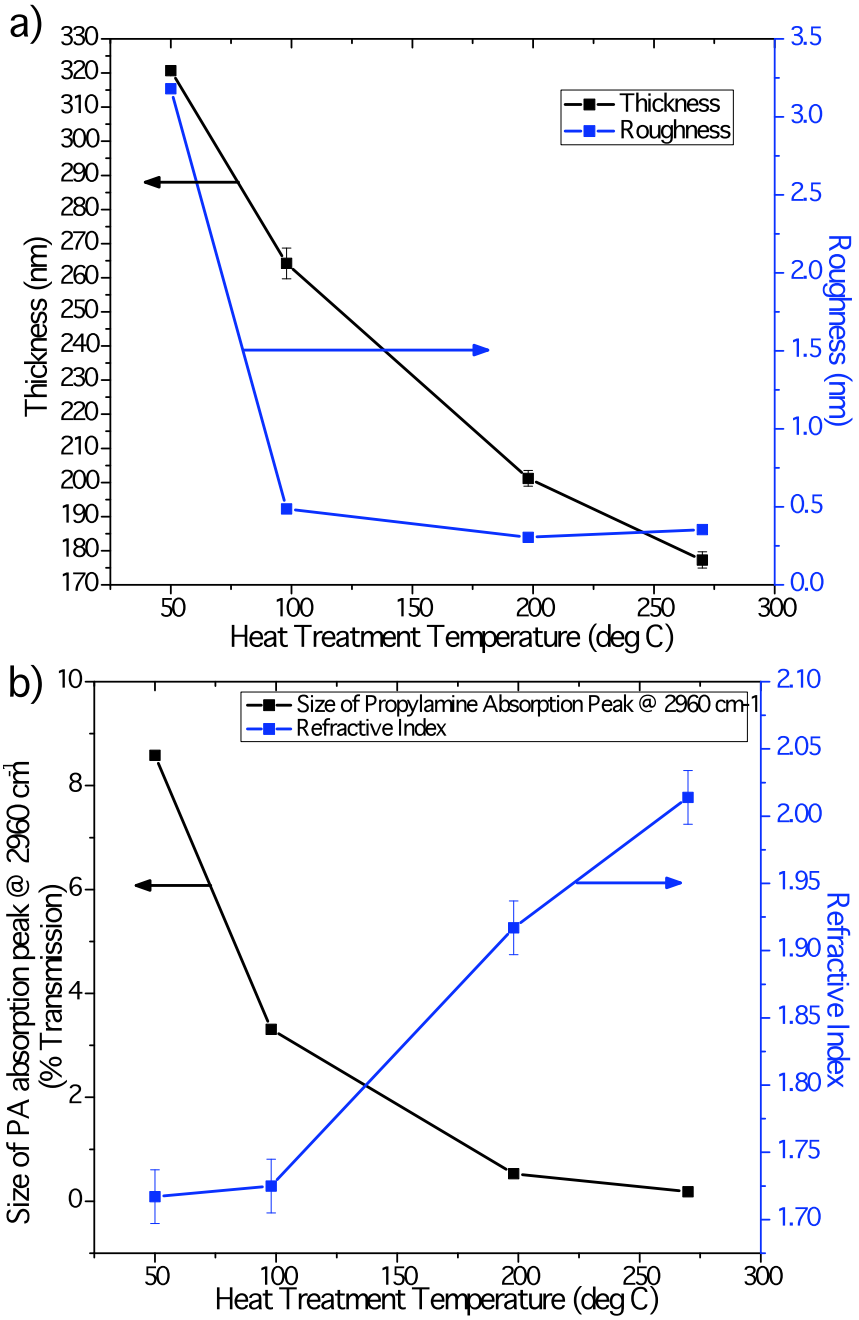

Figure 6.19: Changes in the (a) thickness and roughness and (b) index and size of the PA absorption peak of spin-coated $Ge_{23}Sb_7S_{70}$ films with increasing heat treatment temperature.

Over the course of the heat treatment, the thickness of the film can be seen to reduce to slightly over half of its original value. As this much material is removed from

the films, it is understandable that pinholes are formed on the surface if solvent removal rates are high and there is stress built up in the film or if solvent from deeper in the film has not escaped prior to film consolidation. The thickness decreases almost linearly over the course of the heat treatment, even though almost 2/3 of the residual solvent is removed after baking at 98°C. The refractive index does not increase significantly until after the film has been baked at 198°C. These results support the idea that pores are formed as the solvent is removed at 98°C and heat treatments at higher temperature help to close the pores and densify the films. However, all of the pores are not closed and these appear reach the surface and appear as pinholes as the thickness is reduced. An important factor in analyzing the roughness values is the pinholes in the films heat treated at 198 and 270°C. Looking at the surface profiles presented in Figures 6.16-6.18 and disregarding the pinholes, the differences in roughness appear to be minimal.

6.5 Summary of Findings

In this chapter, the effects of increasing heat treatment temperatures on residual solvent removal as well as structural, optical, and physical properties was studied in detail. The results can be summarized as follows:

- Approximately 99% of the residual solvent that remains in the film after a soft-bake at 50°C can be removed by the proposed multi-step heat treatment: 1 hour at 98°C, 20 minutes at 162°C, 20 minutes at 180°C, and 20 minutes at 198°C.

- As solvent is removed from the film, the glass structure changes from Q_2 units to a mixture of Q_3 and Q_4 units. The Q_4/Q_3 ratio increases with increasing heat treatment temperature.
- The band gap decreases with increasing heat treatment temperature but after heat treatments up to 180°C, it remains higher than the band gap of TE films.
- As solvent is removed from the films, it leaves behind pores. At higher temperatures, many of these pores are closed, leading to an increase in the refractive index as the film is consolidated. This is confirmed by the fact that the thickness continues to decrease significantly even when only a small amount of solvent remains.
- The roughness of the films following the multi-step heat treatment is less than 0.4 nm, well below the target goal of 1.6 nm. However, the presence of pinholes could reduce optical quality.

6.6 References

1. Lin-Vien D, Colthup NB, Fateley WG, and Grasselli JG. *The Handbook of Infrared and Raman Characteristic Frequencies of Organic Molecules*. Academic Press, Inc: San Diego, CA (1991).
2. Petit L, Carlie N, Adamietz F, Couzi M, Rodriguez V, and Richardson KC. Correlation between physical, optical, and structural properties of sulfide glasses in the system Ge-Sb-S. *Materials Chemistry and Physics*. **97**, 64-70 (2006).
3. Charpentier F, Dussauze M, Cathelinaud M, Delaizir G, Kamitsos EI, Adam J-L, Bureau B, and Nazabal V. Aging process of photosensitive chalcogenide films deposited by electron beam deposition. *Journal of Alloys and Compounds*. **509**, 7330-7336 (2011).
4. Zhou ZH, Nasu H, Hashimoto T, and Kamiya K. Non-linear optical properties and structure of Na_2-GeS_2 glasses. *Journal of Non-Crystalline Solids*. **215**, 61-67 (1997).

5. Musgraves JD, et al. Comparison of the optical, thermal and structural properties of Ge-Sb-S thin films deposited using thermal evaporation and pulsed laser deposition techniques. *Acta Materialia*. **59**, 5032-5039 (2011).
6. Waldmann M, Musgraves JD, Richardson K, and Arnold CB. Structural properties of solution processed $Ge_{23}Sb_7S_{70}$ glass materials. Submitted to *Journal of Materials Chemistry* (2012).

CONCLUSIONS

The goal of this work was to fabricate solution-derived thin films with structure and optical properties matching the parent bulk glass and roughness and surface quality comparable to that of TE films. The main questions that this thesis addressed are:

1. How does water affect the glass solutions and the resulting quality and structure of spin-coated films?
2. How can most, if not all, of the residual solvent be removed from the films? What heat treatment times and temperatures are necessary and how do these variables influence post-processed film quality and properties?
3. How does the solvent interact with the glass network and how do these interactions change as solvent is removed?
4. How does residual solvent affect the optical (refractive index, band gap) and physical (roughness, thickness, surface quality) properties of the resulting post-processed films?

The role of water content of the solvent on solution-based film processing was studied for As_2S_3, $Ge_{23}Sb_7S_{70}$, and $Ge_{23}Sb_4S_{73}$. Water content was found to influence dissolution of the glass and can thus affect the surface quality of the post-processed films. While spin speed was found to play a small role, glass loading was the key parameter for controlling the thickness of spin-coated films.

The residual solvent remaining in the films after a soft-bake at 50°C was found to be effectively removed by the following multi-step heat treatment: 1 hour at 98°C, 20

minutes at 162°C, 20 minutes at 180°C, and 20 minutes at 198°C. The propylamine interacts with the glass network by creating non-bridging sulfur atoms in the GeS_4 tetrahedral units. The non-bridging sulfurs are linked to propylamine molecules, as indicated by the presence of SH and R-NH_3^+ absorption bands in the mid-IR spectra. As the solvent is removed from the film, the glass structure was found to change from Q_2 units to a mixture of Q_3 and Q_4 units. The Q_4/Q_3 ratio increased with increasing heat treatment temperature. As solvent is removed from the films, it leaves behind pores. At higher temperatures, many of these pores are eliminated, leading to an increase in the refractive index as the film is consolidated. This is confirmed by the fact that the thickness continues to decrease significantly even when only a small amount of solvent remains.

While the refractive index of the films was increased significantly over the course of the heat treatment, the final value of n = 2.01 is still below the refractive index of the bulk glass, which is n = 2.19. The band gap decreased with increasing heat treatment temperature but after heat treatments up to 180°C, it remained higher than the band gap of TE films. The roughness of the films following the multi-step heat treatment is less than 0.4 nm, well below the target goal of 1.6 nm. However, the presence of pinholes could reduce optical quality.

The target thickness value of 800 nm was reached by increasing the glass loading level of the parent solution, as discussed in chapter 5. These thick films had relatively low rms roughness values typically below 5 nm. However, these thick films have not been optimized for solvent removal. The films deposited in Bordeaux and discussed in

Chapter 6 were optimized for solvent removal but were significantly thinner than films deposited in Clemson. One cause of the reduced thickness of the films deposited in Bordeaux was the high acceleration rate of the spin coater, which could not be adjusted. For the films with 99% of the residual solvent removed and rms roughness values below 0.5 nm, the final thickness was less than 200 nm so the target thickness did not reach the 800 nm goal. These experiments should be repeated on thicker films using a spin coater with an adjustable acceleration rate.

FUTURE WORK

There are many opportunities to build upon the work presented in this thesis. One focus should be on the fabrication of thicker films with the appropriate structure and properties. There are a few different methods that could be used to achieve this goal. One of those methods is to identify a solvent/glass combination that can sustain a higher glass loading level. This could be beneficial because of a lower initial solvent to glass ratio, however, the increased thickness may make it difficult for solvent trapped in the network to reach the surface and be removed from the film. Another method is to deposit multi-layer films. Each layer would undergo the multi-step heat treatment before depositing the next layer. The difficulty with this method is that it is possible that interfaces would be created between the layers, which would reduce optical quality. Thicker films would also allow the use of Raman spectroscopy as a complementary technique to IR spectroscopy for studying the glass network structure. Raman measurements were not possible in this study due to the low thickness of the films.

Future work should also focus on the reduction and, ultimately, the elimination of the pinholes seen on the surface of the final post-processed films. The pinholes do not appear until late in the heat treatment process, so some adjustments to the times and temperatures of the hard bake may be beneficial. While extended periods of time at temperatures above 270°C may allow the glass to flow enough to eliminate the pinholes, this may be at the cost of volatilizing glass components, especially sulfur. However, thermal reflow—holding the glass at a temperature above the T_g for a very short amount

of time—should be tried in an attempt to improve the surface quality without volatilization. Measurements should be performed on films with heat treatment temperatures between 100 and 200°C in order to more fully investigate the evolution of the structure, surface quality, and optical properties over the course of the heat treatment.

APPENDICES

Appendix A

Thin Film Fabrication Techniques

The process for fabricating thin films by thermal evaporation is described in [1] and [2]. Bulk glass of the target material is crushed into a powder and then put into a vessel known as a "boat". The boat is then placed in a vacuum chamber with a clean substrate above it. The boat is heated electrically to above the melting temperature of the target material so the material vaporizes. Once the vapor pressure reaches a desired value, the cool surface of the substrate is exposed and the vapor condenses on it. The thickness of the film can be controlled by the starting amount of material in the boat. An advantage of this method is the high purity of the films due to the high vacuum. One disadvantage is the high cost due to the high temperature and vacuum requirements. Another disadvantage is that it can be difficult to control film composition because of different components volatilizing at different temperatures.

Pulsed laser deposition is similar to TE because both involve a vapor of the target material condensing on a cool substrate and both processes are performed under vacuum. As described in [1,3-4], PLD differs because a high-power short-pulse laser is used to ablate a bulk piece of the target material. This causes some of the material to vaporize and the vapor condenses on the substrate to form a thin film. The experimental setup for PLD is shown in Figure A-1. While films can be prepared relatively quickly and with good stoichiometry using the PLD technique, there are several drawbacks such as non-uniform film thickness, the presence of particles in the film, and the high cost of the process [4].

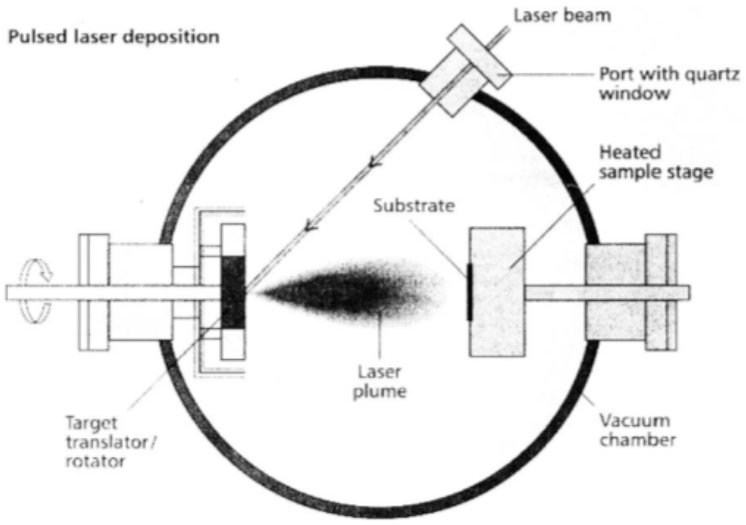

Figure A-1: Experimental setup for pulsed laser deposition, taken from reference [4]

The process of depositing films using chemical vapor deposition is described in detail in [5]. The starting material for this technique is not bulk glass material. Instead, the film is formed through chemical reactions of gaseous precursors. When the gases reach the deposition chamber, they undergo one or more reactions and form intermediate species. Theses species are then absorbed onto the heated substrate. A chemical reaction occurs at the gas-solid interface with the substrate and the film is formed. By-products of the reactions, as well as any unreacted precursors, exit through the exhaust. The experimental setup for depositing Ge-Sb-S films using chemical vapor deposition is shown in Figure A-2. In this case, H_2S is the reactive gas and argon is the carrier gas that brings the glass precursors, $GeCl_4$ and $SbCl_5$, to the deposition chamber. There are many advantages to using CVD. The films produced are pure, uniform, and highly dense and the process can be used for many different materials due to a wide range of chemical precursors [5]. However, as with any process, there are drawbacks as well. Many of the

precursor gases are hazardous and it can also be difficult to control the stoichiometry of the films when using more than once precursor because they have different rates of vaporization [5].

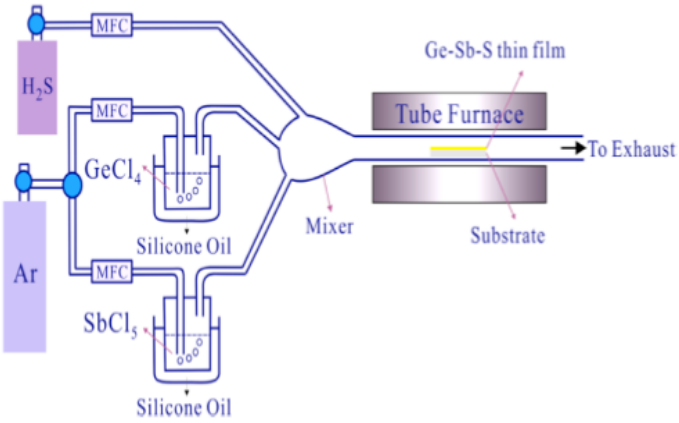

Figure A-2: Experimental setup for chemical vapor deposition, taken from reference [6]

The process of depositing films by sputtering is described in detail in [7]. Inside a vacuum chamber, the substrate is placed on the anode and the target material is placed on the cathode. The chamber is filled with the sputtering gas, which is typically Argon. A voltage is applied and Ar+ ions are formed. The surface of the target material is bombarded with the ions. When these energetic particles hit the target surface, they scatter some of the particles. The scattered particles then deposit on the substrate as a thin film. The experimental setup for sputtering is shown in Figure A-3. Advantages of the sputtering process include the ability to deposit films that are high quality and have good compositional uniformity and the process is widely used commercially [8]. Another advantage is that the source material does not need to be heated [7].

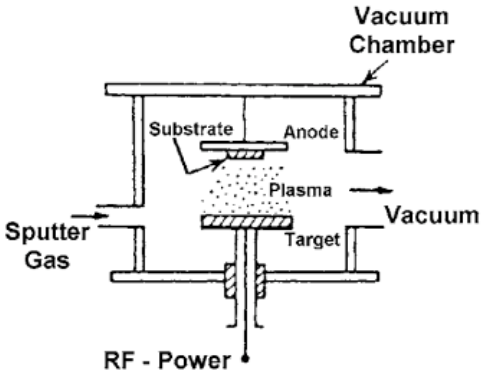

Figure A-3: Experimental setup for RF-diode sputtering system [7]

References

1. Musgraves JD, et al. Comparison of the optical, thermal and structural properties of Ge-Sb-S thin films deposited using thermal evaporation and pulsed laser deposition techniques. *Acta Materialia*. **59**, 5032-5039 (2011).
2. Márquez E, Bernal-Oliva AM, González-Leal JM, Prieto-Alcón R, and Wagner T. Optical properties and structure of amorphous $(As_{0.33}S_{0.67})_{100-x}Te_x$ and $Ge_xSb_{40-x}S_{60}$ chalcogenide semiconducting alloy films deposited by vacuum thermal evaporation. *Journal of Physics D: Applied Physics*. **39**, 1793-1799 (2006).
3. Rode AV, Zakery A, Samoc M, Charters RB, Gamaly EG, and Luther-Davies B. Laser-deposited As_2S_3 chalcogenide films for waveguide applications. *Applied Surface Science*. **197-198**, 481-485 (2002).
4. Frumar M, Frumarova B, Nemec P, Wagner T, Jedelsky J, and Hrdlicka M. Thin chalcogenide films prepared by pulsed laser deposition – new amorphous materials applicable in optoelectronics and chemical sensors. *Journal of Non-Crystalline Solids*. **352**, 544-561 (2006).
5. Choy KL. Chemical vapour deposition of coatings. *Progress in Materials Science*. **48**, 47-170 (2003).
6. Huang CC, Wu CC, Knight K, and Hewak DW. Optical properties of CVD grown amorphous Ge-Sb-S thin films. *Journal of Non-Crystalline Solids*. **356**, 281-285 (2010).
7. Wasa K, Kitabatake M, and Adachi H. *Thin Film Technology: Sputtering of Compound Materials*. William Andrew, Inc: Norwich, NY. P39-40 (2004).
8. Frantz JA, Sanghera JS, Shaw LB, Villalobos G, Aggarwal ID, and Hewak DW. Sputtered films of Er^{3+}-doped gallium lanthanum sulfide glass. *Materials Letters*. **60**, 1350-1353 (2006).